

2D LDH-MoS₂ Clay Nanosheets: Synthesis, Catalase-mimic Capacity, and Imaging-guided Tumor Photo-therapy

Jiayan Zhao

Second Military Medical University First Hospital: Changhai Hospital

Hang Wu

Shanghai Jiaotong University School of Medicine Xinhua Hospital

Jiulong Zhao

Second Military Medical University First Hospital: Changhai Hospital

Yichen Yin

University of Shanghai for Science and Technology

Zhilun Zhang

University of Shanghai for Science and Technology

Shige Wang

University of Shanghai for Science and Technology

Kun Lin (✉ lin17321171461@163.com)

Second Military Medical University First Hospital: Changhai Hospital

Research

Keywords: LDH, MoS₂, chlorin e6, catalysis, tumor therapy

Posted Date: December 1st, 2020

DOI: <https://doi.org/10.21203/rs.3.rs-113491/v1>

License:   This work is licensed under a Creative Commons Attribution 4.0 International License.

[Read Full License](#)

Version of Record: A version of this preprint was published on February 3rd, 2021. See the published version at <https://doi.org/10.1186/s12951-020-00763-7>.

1 **2D LDH-MoS₂ clay nanosheets: synthesis, catalase-mimic**
2 **capacity, and imaging-guided tumor photo-therapy**

3 Jiayan Zhao,^{a,b,1} Hang Wu,^{c,1} Jiulong Zhao,^a Yichen Yin,^b Zhilun Zhang,^b Shige
4 Wang,^b and Kun Lin^{a*}

5
6 ^a Department of Gastroenterology, Changhai Hospital, Second Military Medical
7 University, No. 168 Changhai Road, Shanghai, 200433, P. R. China

8 ^b College of Science, University of Shanghai for Science and Technology, No. 334
9 Jungong Road, Shanghai, 200093, P. R. China

10 ^c Department of General surgery ,Xinhua Hospital, Shanghai jiaotong University
11 school of medicine , No. 1665 Kongjiang Road, Shanghai, 200433, P. R. China

12
13
14
15
16
17
18
19
20
21 ¹ These authors contributed equally to this work. *To whom correspondence should be
22 addressed email: lin17321171461@163.com (Mr. Lin)

23 **Abstract:** Owing to the hypoxia status of the tumor, the reactive oxygen species
24 (ROS) production during photodynamic therapy (PDT) of the tumor is less efficient.
25 Herein, a facile method which involves the synthesis of Mg-Mn-Al layered double
26 hydroxides (LDH) clay with MoS₂ doping in the surface and anionic layer space of
27 LDH was presented, to integrate the photo-thermal effect of MoS₂ and imaging and
28 catalytic functions of Mg-Mn-Al LDH. The designed LDH-MoS₂ (LMM) clay composite
29 was further surface-coated with bovine serum albumin (BSA) to maintain the colloidal
30 stability of LMM in physiological environment. A photosensitizer, chlorin e6 (Ce6), was
31 absorbed at the surface and anionic layer space of LMM@BSA. In the LMM
32 formulation, the magnetic resonance imaging of Mg-Mn-Al LDH was enhanced thanks
33 to the reduced and acid microenvironment of the tumor. Notably, the ROS production
34 and PDT efficiency of Ce6 were significantly improved, because LMM@BSA could
35 catalyze the decomposing of the overexpressed H₂O₂ in tumors to produce oxygen.
36 The biocompatible LMM@BSA that played the synergism with tumor
37 microenvironment is a promising candidate for the effective treatment of cancer.

38

39

40

41

42

43

44 **Keywords:** LDH, MoS₂, chlorin e6, catalysis, tumor therapy

45

46

47 **1. Introduction**

48 The methodology of the detection and medical treatment of cancer has seen
49 a rapid growth over the past few decades.[1-3] However, standard clinical therapies of
50 cancer remain with many defects and individual bottlenecks. Surgical resection would
51 cause operative wounds, X-ray exposure may bring serious side effects to healthy
52 tissue because of off-target,[4, 5] and chemotherapy usually shows limited efficacy
53 with severe multi-drug resistance.[6-8] Thence, the malignant tumor is still posed as
54 one of the greatest enemies of public health,[9, 10] and novel tumor therapeutic
55 approaches to maximizing the treatment efficiency and minimizing the trauma to
56 normal tissue were actively designed. Photon induced tumor therapy, including
57 photothermal therapy (PTT) and photodynamic therapy (PDT), has gained increasing
58 interests in recent years. Tumor PTT relies on the foundation of a photo-thermal
59 transforming agent (PTA) which is capable of transferring the near-infrared (NIR) laser
60 into heat.[11-14] Promisingly, MoS₂ has been extensively explored as a PTA owing to
61 its facile fabrication, admirable bio-compatibility, and high photo-thermal conversion
62 efficiency.[15, 16] As another aspect of photon-induced tumor therapy, PDT primarily
63 involves the killing of cancer cells using the cytotoxic reactive oxygen species (ROS),
64 like singlet oxygen (¹O₂). The ROS could be produced when the photosensitizer (PS)
65 and intra-tissue oxygen are irradiated by external light.[17] The applications of
66 different kinds of nano-platforms such as gold nanomaterials,[18-21] graphene,[22-24]
67 and conjugated polymer-composites[25] to load PS (e.g., chlorin e6, Ce6) for the
68 synergistic tumor PDT and PTT has been extensively studied. However, owing to the

69 hypoxia status of tumors, the ROS production is limited, leading to an unsatisfactory
70 tumor PDT efficiency.[26, 27]

71 As a kind of frequently studied bio-degradable contrast agent, manganese-based
72 nanomaterials could produce numerous Mn (II) paramagnetic centers to enhance the
73 T₁-weighted MR imaging performance of tumors.[28, 29] More importantly,
74 manganese-based nanomaterials could catalyze the decomposing of the
75 over-expressed hydrogen peroxide (H₂O₂) to generate oxygen in tumor and alleviate
76 the tumor hypoxia conditions.[30] Many kinds of clay materials are characterized with
77 layer structure and the interlayer space of the clay has been extensively studied for
78 effective drug encapsulation.[31] Layered double hydroxides (LDHs), accompanying
79 with particular physical properties such as high surface area, acidity, and structural
80 stability, is a class of two dimensional (2D) anionic nano-clay with positive-charged
81 layers.[32-34] The internal galleries of LDHs could exchange with other ions in the
82 external environment.[35] Moreover, their physicochemical properties could be
83 adjusted by modulating the ratio of metallic cations and the sort of interlayer
84 anions.[36-38] Recently, the fabrication of LDH-based clay nanocomposites has
85 gained ever-increasing interests. For example, copper (Cu(II)) or cobalt (Co(II))
86 sulfamerazine-salicylaldehyde complexes were used to intercalate the Mg-Al-LDH
87 that was synthesized by a co-precipitation route.[39] In this research, Mg-Al-LDH
88 composite, which exhibited promising antimicrobial activity against both gram-positive
89 (*Staphylococcus aureus*) and gram-negative (*Escherichia coli*) bacteria, was prepared
90 via a two-step delaminating/restacking method. These motivate us to take the

91 challenge of fabricating an LDH-based composite nano-platform to incorporate the
92 photo-thermal effect of MoS₂ for the imaging-guided combined tumor therapy.

93 Herein, a facile hydrothermal synthesis of LDH-MoS₂ (LMM) clay nanosheets
94 was proposed. The LMM nanosheets were then surface coated with bovine serum
95 albumin (BSA) to gain the colloidal-stability and biocompatibility in vitro and in vivo.
96 Protein/peptide has been frequently used as the template for the biomimetic
97 mineralization, and has been demonstrated to be an efficient and promising strategy
98 for synthesis of nanoparticles for bioapplications.[40] In this LMM@BSA formulation,
99 the photo-thermal transforming agent (i.e., MoS₂) was distributed on the surface and
100 anionic layer space of LDH anionic layer-space the as-designed LDH. MoS₂ provides
101 the possibility to suppress the tumor cell malignant proliferation via NIR laser-induced
102 hyperthermia. At the same time, Mn element renders the LMM@BSA clay nanosheets
103 the tumor reducibility and acidity responsive MR imaging and catalase-mimic
104 capacities to catalyze the disproportionation of H₂O₂. The generated oxygen could
105 alleviate the tumor hypoxia conditions to enhance the production of ROS during PDT.
106 The LMM@BSA clay nanosheets were used to efficiently load the photosensitizer Ce6,
107 which could play the synergism with the catalase-mimic capacity of LMM@BSA to
108 enhance the tumor PDT efficiency. To the best of our knowledge, the synthesis of
109 LDH-based nanocomposites with imaging capacity for combined tumor photo-therapy
110 has not been reported yet.

111

112 **2. Experimental Section**

113 **2.1. Synthesis of LMM@BSA clay nanosheets**

114 All the distilled water applied in this study with a resistivity higher than 18.2 MΩ
115 was produced using a Milli-Q Plus 185 water purification equipment (Millipore,
116 Bedford, MA). The layered LMM nanosheets were synthesized via a hydrothermal
117 method. Firstly, 0.164 g $\text{Mg}(\text{NO}_3)_2 \cdot 6\text{H}_2\text{O}$ (Adamas-beta, Shanghai, China), 0.04 g
118 $\text{Mn}(\text{NO}_3)_2 \cdot 4\text{H}_2\text{O}$ (Adamas-beta, Shanghai, China), and 0.06 g $\text{Al}(\text{NO}_3)_3 \cdot 9\text{H}_2\text{O}$
119 (General Reagent, Shanghai, China) were dissolved together in 10 mL distilled water.
120 The formed aqueous solution was quickly mixed with 20 mL NaOH (Aladdin,
121 Shanghai, China, prepared into 0.15 mol/L solution). After one hour of magnetic
122 stirring at room temperature, the solution was centrifuged (8000 rounds/min, 5 min) to
123 collect the sediment. The sediment was then dissolved into 25 mL distilled water and
124 then mixed with 10 mL $(\text{NH}_4)_2\text{MoS}_4$ (J&K Chemical, Shanghai, China) aqueous
125 solution (5 mg/mL) and magnetically stirred for 1.5 h (600 rounds/min). After sealed
126 into a 100 mL stainless steel autoclave that lining with polyphenylene, the mixture was
127 heated in an oven at 180°C for 12 h. Then, the product was thoroughly water-washed
128 for three times and centrifuged (8000 rounds/min, 5 min) to get LMM clay nanosheets.
129 The Mg-Al-LDH nanosheets preparation was similar to the synthesis of LMM
130 nanosheets but without the addition of $\text{Mn}(\text{NO}_3)_2 \cdot 4\text{H}_2\text{O}$. The sediment was dissolved
131 into 35 mL distilled water. The formed LMM clay nanosheets and Mg-Al-LDH
132 nanosheets were lyophilized for future use. To prepare LMM@BSA clay nanosheets,
133 10 mg freeze-dried powder of LMM was dispersed in 10 mL distilled water with 250
134 mg BSA (Aladdin, Shanghai, China). The product then underwent an ultrasonic
135 shattering (500 W, 120 min), centrifugation (13000 rounds/min, 10 min), and twice
136 water-washed. The product was dissolved into 10 mL distilled water for further

137 application.

138 **2.2. Material characterization**

139 The surface morphology of LMM nanosheets was recorded using a scanning
140 transmission electron microscopy (SEM, FEI Magellan 400). The microstructure of
141 LMM@BSA clay nanosheets was observed by a transmission electron microscopy
142 (TEM, FEI Tecnai G2 F20). Before the SEM and TEM observation, LMM nanosheets
143 was dissolve in water with a concentration of 100 $\mu\text{g}/\text{mL}$. The distribution of Al, Mg,
144 Mo, Mn, O and S in the LMM nanosheets was mapped with the Energy-dispersive
145 X-ray spectroscopy (as the accessory of TEM). The chemical nature of LMM material
146 was characterized by X-ray photoelectron spectroscopy (XPS, Thermal Scientific
147 ESCAlab250). The test results were calibrated by the C1s peak (284.8 eV). X-ray
148 diffraction (XRD, Rigaku D/max-2200 PC) system was used to assess the crystalline
149 structures of LDH and LMM nanosheets (operation parameters: Cu $K\alpha$ radiation, the
150 wavelength at 1.54 \AA , scanning from 5° to 70° (2θ)). The scanning voltage and current
151 was set as 40 kV and 40 mA, respectively). The chemical information of BSA and
152 freeze-dried powder of LMM and LMM@BSA was determined by a Fourier Transform
153 Infrared (FTIR) spectroscopy under the transmission mode in the wavelength range of
154 4000 to 500 cm^{-1} (Nicolet 7000-C spectrometer). The dynamic light scattering (DLS)
155 diameters of LMM@BSA clay nanosheets in various solutions were also measured
156 (Malvern Nano ZS90 Zetasizer Nano series). The mass ratio of surface-modified BSA
157 was determined using thermogravimetric (TG209F1 system, NETZSCH Instruments
158 Co., Ltd., Germany). Samples were heated from 50°C to 900°C with a heating rate of
159 $20^\circ\text{C}/\text{min}$ under air atmosphere. The UV-vis-NIR spectrometer (Lambda 25, Perkin

160 Elmer, USA) was used to record the light absorption of nanosheets.

161 **2.3. In vitro photo-thermal performance**

162 The in vitro photo-thermal performance of the LMM@BSA clay nanosheets was
163 studied by continuously irradiating the nanosheets solution with 808 nm NIR laser
164 (Shanghai Connet Fiber optics Company). The distance between the sample and the
165 emitting end of NIR laser was 15 cm. To study the influence of materials concentration
166 on the photothermal conversion, a cell culture plate (96-well) of LMM@BSA clay
167 nanosheets solutions at various concentrations (0 (distilled water, control), 50, 100,
168 and 250 $\mu\text{g}/\text{mL}$) was irradiated with NIR laser ($1.0 \text{ W}/\text{cm}^2$) for a duration of 5 min. To
169 study the influence of power density on the photothermal conversion, LMM@BSA clay
170 nanosheets ($500 \mu\text{g}/\text{mL}$) were irradiated with NIR laser ($0.2 \text{ W}/\text{cm}^2$, $0.5/\text{cm}^2$, $0.8/\text{cm}^2$
171 and $1.0 \text{ W}/\text{cm}^2$) for a duration of 5 min. The temperature changes (ΔT) and the
172 related thermal images were recorded using a FLIR™ E60 infrared camera. To prove
173 the photo-thermal stability of the LMM@BSA clay nanosheets, 100 μL solution was
174 irradiated with NIR laser (808 nm), and its ΔT s in 10 cycles (laser on/off in turn) were
175 plotted. The photo-thermal conversion efficiency (η) of the LMM@BSA clay
176 nanosheets was ascertained with a modified Korgel's research method,[41, 42]
177 whose value could be calculated as follows:

$$178 \quad \eta = \frac{hS(T_{max} - T_{Surr}) - Q_{in,Surr}}{I(1 - 10^{-A\lambda})} * 100\% \quad (1)$$

179 In this formula, S denotes the irradiated surface area of nanosheets. hS
180 could be determined by measuring the temperature dropping-speed since the
181 beginning of the laser-off. T_{max} refers to the highest temperature of the
182 nanosheets solution. T_{surr} is the ambient temperature. $Q_{in,surr}$ implies the heat

183 transferred to the surrounding. I and A (λ) respectively represent the laser
184 power (in Watt) and the absorbance of the LMM@BSA clay nanosheets at 808
185 nm.

186 **2.4. In vitro cytocompatibility**

187 At the incubation conditions (37°C and 5% CO₂), L929 cells (bought from Institute
188 of Biochemistry and Cell Biology, the Chinese Academy of Science, Shanghai, China)
189 were cultivated in DMEM which contained 100 µg/mL streptomycin, 100 U/mL
190 penicillin and 10% fetal bovine serum. To assess the in vitro biocompatibility, the L929
191 cells were seeded into a cell culture plate (96-well, 8 × 10³ cells/well). After cultured
192 for 12 h, the old medium was replaced with LMM@BSA clay nanosheets solution (500,
193 250, 100, 50, and 0 µg/mL (control) in DMEM). After a 24-h incubation, the DMEM and
194 materials were discarded. Cells were washed with PBS for 3 times and the metabolic
195 activity and morphology of the L929 cells were evaluated by a cell counting kit-8
196 (CCK-8, Dojindo, Japan) and Live/Dead staining (LIVE/DEAD™ Cell Vitality Assay Kit,
197 ThermoFisher Technologies, USA) according to the instructions. The live cells stain in
198 green and the dead cells stain red. The stained cells were photographed using a
199 Leica DM IL LED (Germany) inverted phase-contrast microscope.

200 Mice red blood cells (mRBCs) were centrifuged from the serum and washed with
201 saline for 3 times. Thereafter, mRBCs were stored in PBS at 4°C. Upon experiment,
202 0.2 mL mRBC suspension was evenly dispersed in three 1.5-mL Eppendorf tubes with
203 0.8 mL distilled water, saline, or LMM@BSA clay nanosheets (in saline) respectively.
204 The final concentrations of the nanosheets are 50, 100, 200, and 500 µg/m. The
205 mixtures were cultured for 2 h at 37°C and centrifuged (5000 rounds/min, 3 min). The

206 absorbance of the supernatants at 541 nm was detected using the UV-vis-NIR
207 spectrometer (Lambda 25, Perkin Elmer, USA). The hemolytic percentage (HP) was
208 derived in the equation (2):

$$209 \quad \text{HP (\%)} = \frac{(A_t - A_{nc})}{(A_{pc} - A_{nc})} \quad (2)$$

210 In this formula, A_{nc} , A_{pc} , and A_t are absorbance values of PBS, water, and
211 LMM@BSA clay nanosheets treated blood supernatant, respectively.

212 **2.5. Ce6 loading and singlet oxygen detection**

213 The LMM@BSA and Ce6 were magnetically stirred for 24 h at room temperature
214 in dark. The final concentration of LMM@BSA was 100 or 500 $\mu\text{g/mL}$, and the final
215 Ce6 concentration was 10, 50, or 100 $\mu\text{g/mL}$. Then, the mixture was centrifuged
216 (12000 rounds/min, 10 min) to separate the superfluous Ce6. The sediment was
217 washed with distilled water for 3 times, and the loading efficiency of Ce6 could be
218 determined according to the UV-vis-NIR spectra absorbance of these liquids, using
219 the standard curve of Ce6 at 403 nm. The loading efficiency was calculated in
220 accordance with the formula (3):

$$221 \quad \text{Loading efficiency (\%)} = \frac{C_0 - C_s}{C_0} * 100\% (3)$$

222 In this formula, C_0 is the total concentration of Ce6, and C_s is the Ce6
223 concentration in the supernatant.

224 A JPB-608 dissolved oxygen analyzer (Shanghai INESA Scientific Instrument
225 Company) was used to quantize the dissolved oxygen (DO) content in LMM@BSA
226 clay nanosheets solution. To this end, the electrode immersed in LMM@BSA clay
227 nanosheets (500 $\mu\text{g/mL}$) solution with or without H_2O_2 (50 mM). These solutions were
228 hand-shaken at 20-40 cm/second. The DO values were record by the analyzer at an

229 interval of 30 seconds in a total duration of 10 min. The singlet oxygen ($^1\text{O}_2$) produced
230 by the Ce6 loaded nanosheets was probed using 1,3-diphenylisobenzofuran (DPBF).
231 In detail, 50 μL DPBF (10 mM in ethanol) was added into the LMM@BSA/Ce6 aqueous
232 solution (2.95 mL, 1 mg/mL) with the absence or presence of H_2O_2 (final concentration
233 50 mM). The absorption spectra of the mixed solution were recorded every 5 min
234 during the 660 nm laser irradiation (30 min, 0.1 W/cm^2) using the UV-vis-NIR
235 spectrometer (Lambda 25, Perkin Elmer, USA).

236 **2.6. In vitro tumor therapy**

237 **2.6.1 In vitro tumor PTT**

238 Human colorectal carcinoma (HT29) cells (obtained from Institute of Biochemistry
239 and Cell Biology, the Chinese Academy of Science, Shanghai, China) were seeded in
240 a 96-well plate (8×10^3 cells/well) containing 100 μL DMEM per well overnight. Next,
241 the fresh medium with LMM@BSA clay nanosheets (0 (PBS), 50, 100, 250, and 500
242 $\mu\text{g}/\text{mL}$) was substituted for the pure medium and the cells were cultured for 4 h. Then,
243 the cells were irradiated with 808 nm laser for 5 min. To study the influence of power
244 density on the cell viability, the cells cultured with 500 $\mu\text{g}/\text{mL}$ LMM@BSA clay
245 nanosheets were cultured for 4 h and then irradiated with 808 nm NIR laser (0.2, 0.5,
246 0.8, and 1.0 W/cm^2) for 5 min. The metabolic activity and morphology of the L929 cells
247 were evaluated by a cell counting kit-8 (CCK-8, Dojindo, Japan) and Live/Dead
248 staining.

249 **2.6.2 In vitro tumor PTT and PDT**

250 To study the irradiation time-dependent tumor PDT, cells (5 groups) were cultured
251 with LMM@BSA/Ce6 nanosheets (LMM@BSA: 100 $\mu\text{g}/\text{mL}$; Ce6: 10 $\mu\text{g}/\text{mL}$) and

252 cultured for 4 h. Then, the alternated irradiation of 660 nm laser (0.1 W/cm^2) were
253 applied to the cells (group I: without irradiation, control; group II: 1 min; group III: 2
254 min; group IV: 3 min; group V: 5 min). To study the combined tumor PTT and PDT,
255 cells were cultured with LMM@BSA clay nanosheets (group I and II, $100 \mu\text{g/mL}$) or
256 LMM@BSA/Ce6 (group III and IV, $100 \mu\text{g/mL}$ LMM@BSA, $10 \mu\text{g/mL}$ Ce6). Then, the
257 alternated irradiation of 660 nm laser (0.1 W/cm^2) and 808 nm laser (1.0 W/cm^2) were
258 applied to the cells (group I: without irradiation; group II: 808 nm, 5 min; group III: 606
259 nm, 5 min; group IV: 606 nm, 5 min, and 808 nm, 5 min). The metabolic activity and
260 morphology of the L929 cells were evaluated by a cell counting kit-8 (CCK-8, Dojindo,
261 Japan) and Live/Dead staining.

262 **2.7. In vivo biocompatibility**

263 The in vivo studies were performed in Changhai Hospital, Second Military Medical
264 University. The animal-handling was in accordance with the policies of the National
265 Ministry of Health. KM mice (SPF level, Shanghai Slac Laboratory Animal Center,
266 China) were intravenously (I.V.) injected with $200 \mu\text{L}$ LMM@BSA clay nanosheets
267 solution (3 mg/mL , in saline). Another group injected with $200 \mu\text{L}$ saline was set as
268 control. These mice were euthanized on the 1st d, 7th d, and 14th d. The body weight of
269 KM mice was about 20 g. Therefore the injected dosage of LMM@BSA clay
270 nanosheets to mice could be determined as about 30 mg/kg . Major organs (kidney,
271 lung, spleen, liver, and heart) of these mice were weighed and aqua regia was used to
272 thoroughly digest these weighed organs for 3 days to quantify their respective
273 contents of Mn ions with an Agilent ICP-OES (700 Series). The KM mice body weights
274 were also monitored during the experiment. Standard hematoxylin-eosin (H&E)

275 dyeing was introduced to assess the in vivo biosafety of the LMM@BSA clay
276 nanosheets with the help of a Leica DM IL LED inverted phase-contrast microscope.

277 For the in vivo hemocompatibility assessment, the routine blood test (using
278 Sysmex XS-800i automated hematology analyzer) and serum biochemistry test (using
279 Beckman Coulter Unicel DxC 800 automatic biochemical analyzer) were performed
280 as follows: KM mice I.V. administered with 200 μ L saline (set as control) or
281 nanosheets solution (3 mg/mL) were anesthetized by puncturing the heart for
282 blood-drawing on the 1st, 7th, and 14th day post-injection.

283 **2.8. In vitro and in vivo MR imaging**

284 The Mn content in 20 mg LMM@BSA clay nanosheets (digested in aqua regia)
285 was firstly ascertained by an Inductive Coupled Plasma Emission Spectrometer (ICP).
286 LMM@BSA clay nanosheets solutions at a gradient Mn concentration (1.0 mL, Mn
287 concentration: 0.2 mg/mL, 0.5 mg/mL and 1.0 mg/mL) in three solvents, namely
288 distilled water, GSH, and citric acid buffer (pH = 5.0) and incubated for 2 h. Then,
289 T₁-weighed MR imaging was finished on an MR imaging system (GE Signa 3.0 T,
290 imaging parameters: TR = 600 ms; TE = Min Full; bandwidth = 15.63 kHz; and slice
291 thickness = 3 mm).

292 The nude mice (Shanghai Slac Laboratory Animal Center, Shanghai, China) were
293 subcutaneously injected with 150 μ L serum-free DMEM containing 1×10^7 HT29 cells
294 on their backs for the construction of tumor models. When the tumor grew into ~ 0.5
295 cm³ after approximately two weeks of feeding, the tumor-bearing mice were
296 intratumorally (I.T.) or I.V. injected with the LMM@BSA clay nanosheets (1 mg/mL in
297 saline). These mice were anesthetized and placed in a home-made plate immediately

298 after the I.T. materials injection or 12 h after the I.V. materials injection for the in vivo
299 imaging (imaging parameters: TR = 400 ms; TE = 8.9 ms; Fov = 6 × 6 cm; and slice
300 thickness = 2 mm). The relative brightness intensity (RBI) was calculated based on
301 the equation (4):

$$302 \quad \text{RBI} = \frac{\text{BI}_x}{\text{BI}_o} \quad (4)$$

303 In this formula, BI_x and BI_o represent the brightness intensity of the experimental
304 and control groups in the MR region of interest (area = 5 mm²), respectively.

305 **2.9. In vivo tumor therapy**

306 Tumor-bearing mice were randomized into five groups (n = 3). These mice were
307 I.V. injected with saline (group I, 200 μL), or 200 μL LMM@BSA/Ce6 (group II-IV, 1
308 mg/mL in saline). Members in group V were I.T. injected with 20 μL LMM@BSA/Ce6
309 (in saline). After 12 h, the mice in the group II and III were received the 808 nm (group
310 II, 1.0 W/cm², 5 min) and 660 nm (group III, 0.1 W/cm², 5 min) NIR laser irradiation
311 respectively. The mice in group IV and V were successively irradiated with 660 nm
312 (0.1 W/cm²) and 808 nm (1.0 W/cm²) laser for 5 min. The ΔTs of tumor and the
313 thermal images during treatment were recorded using a FLIR™ E60 camera. At
314 different time points, relative tumor volume (denoted as V/V₀, V₀ and V represent the
315 real-time and initial tumor volume, respectively) and the appearance of each
316 tumor-bearing mouse was recorded.

317 **2.10. Drug loading and release**

318 To load DOX, a stock solution of DOX (10 mg/mL, 20 μL) was added into the
319 LMM@BSA clay nanosheets solution (1 mg/mL) under room temperature and stirred
320 for 24 h in the dark. The product was purified by centrifugation (12000 rounds/min, 10

321 min) and rinsed with water for 3 times. The absorbance of the collected supernatant at
322 480 nm was determined by UV-vis-NIR spectroscopy to calculate the DOX loading
323 quantity according to the concentration-absorbance standard curve of DOX at the
324 same wavelength.

325 The drug release from the LMM@BSA/DOX nanosheets was studied at different
326 pH values and temperatures. In detail, LMM@BSA/DOX solutions were placed in vials
327 containing 5 mL buffer with different pH values (PBS (pH = 7.4) or citrate buffer
328 solution (pH = 6.0)) and incubated at 54°C or 37°C, respectively. At pre-designed time
329 points, 1 mL buffer containing the released DOX was taken out and its absorbance at
330 480 nm was monitored for calculating the real-time released DOX amount. Finally, 1
331 mL fresh buffer was supplanted.

332 **2.11. Statistical analysis**

333 The one way ANOVA statistical analysis was chosen to determine the
334 significance of data, where 0.05 was appointed as the threshold ((*) $p < 0.05$, (**) $p <$
335 0.01 , (***) $p < 0.001$). Unless specified, the sample size is three ($n = 3$) in this study.

336

337 **3. Results and Discussions**

338 **3.1. Materials synthesis and characterization**

339 Unlike the traditional co-precipitation route which involves the two-step nucleation
340 and sediment ageing,[43] the LDH-based clay nanosheets, namely the LMM, was
341 synthesized via hydrothermally treating the mixture solution of NaOH, $(\text{NH}_4)_2\text{MoS}_4$,

342 $\text{Mn}(\text{NO}_3)_2 \cdot 4\text{H}_2\text{O}$, $\text{Mg}(\text{NO}_3)_2 \cdot 6\text{H}_2\text{O}$ and $\text{Al}(\text{NO}_3)_3 \cdot 9\text{H}_2\text{O}$. During the hydrothermal
343 synthesis, $\text{Mn}(\text{NO}_3)_2 \cdot 4\text{H}_2\text{O}$, $\text{Mg}(\text{NO}_3)_2 \cdot 6\text{H}_2\text{O}$ and $\text{Al}(\text{NO}_3)_3 \cdot 9\text{H}_2\text{O}$ were transformed
344 into Mg-Mn-Al-LDH, and $(\text{NH}_4)_2\text{MoS}_4$ was transformed into MoS_2 . The LMM was
345 sonicated in BSA solution for BSA coating to gain colloidal stability in physiological
346 conditions. The as-prepared LMM@BSA clay nanosheets were further used to load
347 Ce6, which could generate the cytotoxic ROS (i.e., $^1\text{O}_2$) upon the 660 nm laser
348 irradiation, for the MR imaging-guided photo-therapy of the tumor (**Scheme 1**). It
349 could be easily observed from the SEM that the as-prepared product presents a 2D
350 structure (Figure 1a, b). The element mapping (Figure 1d-i) further verifies the even
351 coexistence of Al, Mg, Mo, Mn, O, and S in the LMM@BSA clay nanosheets.

352 XPS analysis was introduced to research the valence state of various elements in
353 the nanosheets. The peaks belonging to $\text{Mo}^{4+} 3d^{5/2}$ (at 228.6 eV), $\text{Mo}^{6+} 3d^{5/2}$ (232.0
354 eV) and $3d^{3/2}$ (235.9 eV) (Figure S1a); peaks at 74.7 eV and 1304.1 eV were ascribed
355 to Al $2p^{3/2}$ and Mg 1s respectively were also detected in the XPS spectrum of Mo
356 element (Figure S1b, c). The peak of S^{2-} at 162.18 eV (S $2p^{3/2}$) was observed as well
357 (Figure S1d), confirming that the nanosheets are composed of MoS_2 . In addition, the
358 peaks at 641.2 eV, 653.8 eV, and 641.9 eV represent $\text{Mn}^{3+} 2p^{3/2}$, $\text{Mn}^{3+} 2p^{1/2}$, and Mn^{2+}
359 $2p^{3/2}$ (Figure 2a), respectively, indicating that the valences of Mn are Mn^{3+} and Mn^{2+} .
360 The XPS spectrum of Mn was fitted according to literature and the atom ratio of Mn^{3+}
361 and Mn^{2+} was evaluated to be 50.7:49.3.[44] The structural nature of LMM
362 nanosheets was then studied using XRD (Figure 2b). Compared with Mg-Al-LDH, the
363 typical (003), (006), (012) and (110) peaks at 11.70° , 23.54° , 33.4° , 60.23° ((JCPDS:
364 14-0191) were weakened after doping with MoS_2 (red line: LDH- MoS_2) and even

365 disappeared after further doping with manganese (blue line: LMM). Besides, the (002)
366 peak of MoS₂ (JCPDS: 75-1539, red line: LDH-MoS₂) was also weakened after
367 doping with manganese (blue line: LMM), implying that the doping of Mo and Mn has
368 restricted the growth of the crystalline of Mg-Al-LDH.

369 FTIR was used to confirm the successful BSA coating (Figure 2c). The peaks at
370 3320 cm⁻¹ and 2950 cm⁻¹ represent the asymmetry elastic of -NH₂ and -CH₃ of BSA.
371 Peaks belonging to amide III, II, and I at 1390 cm⁻¹, 1540 cm⁻¹, and 1640 cm⁻¹ could be
372 found in the curve of BSA and LMM@BSA clay nanosheets, revealing the successful
373 coating of BSA. To quantify the amount of surface-coated BSA, LMM, BSA, and
374 LMM@BSA clay nanosheets were programmatically heated to 900 °C in air, which
375 confirms that the mass ratio of surface-coated BSA was approximately 56.4% (Figure
376 2d). The size of LMM@BSA clay nanosheets in DMEM was ~147 nm, and the size
377 fluctuation of DLS during 24 h was ignorable (Figure S2). Moreover, the LMM@BSA
378 clay nanosheets could be well-dispersed in water, PBS, and DMEM and showed the
379 noticeable Tyndall effect (Figure 1c), indicating that the modified BSA molecules
380 endow the nanosheets with excellent colloidal stability in certain circumstances.

381 **3.2. In vitro photo-thermal performance**

382 In line with the MoS₂, [45, 46] the LMM@BSA clay nanosheets demonstrate
383 apparent light absorption that is closely related to their concentration within
384 wavelength from 400 to 1100 nm (Figure 3a). Setting the experimental device
385 according to Figure 3b and under laser irradiation (1.0 W/cm², 5 min), the solution
386 temperatures swiftly increased by 13°C, 21°C, and 33°C corresponding to their
387 concentrations at 50 µg/mL, 100 µg/mL, and 250 µg/mL, respectively. However, under

388 the same circumstance, the distilled water merely increased by 6.5°C (Figure 3c).
389 When irradiating the LMM@BSA clay nanosheets (500 µg/mL) with varied laser
390 power density, the temperatures increased by 44°C, 34°C, 22°C and 9°C upon laser
391 powered at 1.0 W/cm², 0.8 W/cm², 0.5 W/cm² and 0.2 W/cm², respectively. The
392 related thermal picture captured by the FLIR™ camera further reinforced the
393 relationship of photo-thermal performance with irradiation time, power density and
394 material concentration (Figure 3d, f). The photo-thermal efficiency of the LMM@BSA
395 clay nanosheets was figured at 31.6% (Figure 3g and h), which is higher than MoS₂
396 nanospheres [16] and other kinds of MoS₂ based composites (like
397 MoS₂@Fe₃O₄-ICG/Pt(IV) nanoflowers).[15] Moreover, negligible maximum
398 temperature changes after being irradiated by 808 nm laser for 10 cycles were
399 observed, indicating the desirable thermal stability of LMM@BSA clay nanosheets
400 (Figure 3i). Given the outstanding photo-thermal conversion efficiency and thermal
401 durability, it was anticipated that LMM@BSA clay nanosheets are suitable for the
402 tumor hyperthermia treatment.

403 **3.3. In vitro compatibility**

404 The appraisal of in vitro cytotoxicity of LMM@BSA clay nanosheets is
405 fundamental for its biomedical applications. The viability of L929 cells that were
406 cultured with LMM@BSA clay nanosheets for 24 h remained higher than 90% (0-500
407 µg/mL, Figure S3a), with similar morphology to those treated with saline (control,
408 Figure S4a, b). Further, calcein-AM/PI study suggests that the Live/Dead cells
409 staining results were in accordance with CCK-8 assay and the morphology
410 observation evidently proved that the nanosheets would not destruct the integrity of

411 cell membrane in the experimental concentration range (Figure S3b-f).

412 To further prove the hemocompatibility of LMM@BSA, the hemolytic assay was
413 carried out. As calculated, the HPs of experimental samples turned out to be lower
414 than 2% under nanosheets concentration of 0-500 $\mu\text{g/mL}$ (Figure S5), implying the
415 excellent hemocompatibility of LMM@BSA clay nanosheets within the experimental
416 dosage.

417 **3.4. Ce6 loading and detection of $^1\text{O}_2$**

418 The interlayer space and the surface of the LMM@BSA clay nanosheets could
419 contribute to its physical adsorption of drugs or photosensitizers. In this study, the
420 photosensitizer agent, namely Ce6, was mixed with LMM@BSA, after which a
421 characteristic peak at 403 nm belonging to Ce6 was successfully detected in the
422 UV-vis-NIR spectrum of the centrifugal product (Figure S6). This indicates that the
423 Ce6 was successfully loaded on LMM@BSA clay nanosheets. Owing to the increased
424 loading sites, the loading efficiency of Ce6 was found to grow with the
425 increasing-concentration of LMM@BSA clay nanosheets. Besides, the increasing of
426 Ce6 concentration could also raise the Ce6 loading efficiency, and a high loading
427 efficiency of $89.37 \pm 3.92\%$ was obtained when the LMM@BSA and Ce6
428 concentrations were 500 $\mu\text{g/mL}$ and 100 $\mu\text{g/mL}$, respectively (Figure 4a). To confirm
429 the catalytic efficiency of LMM@BSA, the DO content in LMM@BSA solution with and
430 without the addition of H_2O_2 was compared. The introduction of H_2O_2 led to an
431 increase in the DO content of the LMM@BSA solution (Figure 4b), implying that the
432 H_2O_2 has been transformed into O_2 under the catalysis of LMM@BSA. It was worth
433 noting that the obvious lower starting value in the DO content might be corresponding

434 to the H₂O₂-induced degradation of nanosheets, which consumed the oxygen to some
435 extent.

436 To certificate that LMM@BSA could enhance the ROS production of Ce6 under
437 the irradiation of 660 nm laser, the ¹O₂ production of LMM@BSA/Ce6 was studied
438 (Figure 4c-d). The structure of DPBF alters quickly upon strong oxidants such as ROS
439 [17], leading to the apparent decrease of light absorption at 410 nm. Therefore, it was
440 applied to indicate the emergence of ¹O₂. Upon the irradiation with 660 nm laser, the
441 absorption peaks of DPBF at 410 nm were weakened, implying the continuous
442 generation of ¹O₂. Interestingly, the decrease of absorption peak of DPBF at 410 nm
443 was more swiftly after the adding of H₂O₂ (Figure 4d), proving that the ¹O₂ production
444 rate was improved. Such a distinct difference in the absorption peaks decreasing-rate
445 of DPBF suggests that the LMM@BSA could trigger the decomposition of H₂O₂ to
446 produce O₂. These dissolved O₂ molecules took part in the photosensitization of Ce6
447 and then enhanced the production of ROS.

448 **3.5. In vitro combined tumor therapy**

449 The in vitro tumor PTT efficiency was examined with HT29 cells. Upon the laser
450 irradiation, the viability of HT29 cells decreased with the increasing of LMM@BSA
451 clay nanosheets concentration (0-500 µg/mL) and attenuated to 14.2 ± 1.4% when the
452 LMM@BSA clay nanosheets reached 500 µg/mL (Figure S7a). By fixing the
453 LMM@BSA at 500 µg/mL, the HT29 cells' viability declined gradually with the
454 enhancement of power density and a low viability of 14.6 ± 0.1% was found at the
455 laser power density of 1.0 W/cm² (Figure S8a). Consistent with the CCK-8 results, the
456 calcein-AM/PI dyeing further demonstrates that the cellular apoptosis relies on

457 nanosheets concentration and laser power density (Figure S7b-d and S8b-f), giving
458 more evidence that the NIR laser-caused local hyperthermia could inhibit the cellular
459 proliferation. Based on the concentration and power density-dependent tumor-killing
460 effect, LMM@BSA clay nanosheets with a concentration of 100 $\mu\text{g}/\text{mL}$ and 808 nm
461 laser with a power density of 1.0 W/cm^2 were applied for the synergistic tumor
462 therapy.

463 With the proved catalytic activity, LMM@BSA clay nanosheets are anticipated to
464 enhance the tumor PDT efficiency after Ce6 loading. To prove this hypothesis, HT29
465 cells were used as the model to research the in vitro tumor PDT efficiency. The
466 apoptosis extent of HT29 was correlated to the irradiation time, and the cell viability
467 decreased to $40.3 \pm 6.0\%$ after 5 min irradiation, which is consistent with the
468 calcein-AM/PI dyeing outcomes (Figure S9). The cellular viability of HT29 cells treated
469 with LMM@BSA and LMM@BSA/Ce6 nanosheets decreased to $86.6 \pm 1.7\%$ and
470 $41.7 \pm 3.3\%$ respectively after the laser irradiation (Figure 4e-i). Interestingly, the
471 cellular viability of HT29 cells attenuated to $13.8 \pm 1.3\%$ after successively exposed to
472 808 nm and 660 nm laser, clearly indicating the combination of tumor PTT and PDT.

473 **3.6. In vivo compatibility**

474 To assess the in vivo biocompatibility, the body weight of mice (I.V. injected with
475 LMM@BSA) was observed, which showed a normal fluctuation during 14 d feeding
476 (Figure 5a). The routine blood and serum biochemistry tests results displayed
477 negligible statistical differences between the control and the test groups (Figure 5c-d
478 and Figure S10), further revealing the outstanding blood cell safety of the LMM@BSA
479 clay nanosheets. The in vivo biocompatibility was then studied by performing the

480 bio-distribution study of nanosheets. The results proved that the Mn levels in major
481 organs gradually attenuated over the feeding time, indicating that LMM@BSA clay
482 nanosheets could be excreted out of these organs (Figure 5b). The nanosheets'
483 long-term biosafety and histocompatibility were finally tracked by H&E dyeing of
484 major organs (Figure 5e and Figure S11). Compared with healthy mice, the
485 LMM@BSA clay nanosheets neither brought any off-target detriment nor pathological
486 effect to normal organs during the feeding, further supporting the excellent biosafety
487 of nanosheets.

488 **3.7. In vitro and in vivo MR imaging**

489 Manganese-based nanomaterial has been frequently studied as the imaging
490 contrast for T₁-weighted MR imaging. Interestingly, such an imaging capacity was
491 well-inherited by the LMM@BSA clay nanosheets. Moreover, the MR imaging is tumor
492 microenvironment (i.e., mildly acidic and GSH) responsive. The brightness intensity of
493 LMM@BSA clay nanosheets increased with its concentration. Surprisingly, owing to
494 its fast break-up in acidic condition, the imaging pictures of nanosheets dispersed in
495 acidic buffer (pH = 5.0) were brighter than in distilled water. The brightness was
496 detected as 4184, 4236 and 4411 when its concentration was 0.25, 0.50, 1.0 mg/mL,
497 respectively in citric acid buffer (pH = 5.0). In distilled water, however, it was only
498 recorded as 2972, 3060 and 3173. Moreover, the solution brightness in GSH
499 increased to 3274, 3283, and 3681, which is higher than that in distilled water,
500 probably owing to the fast-dissolving and reduction of Mn³⁺ to Mn²⁺ by GSH (Figure
501 6a,b). The MR imaging capacity of LMM@BSA clay nanosheets was further evaluated
502 in vivo on Balb/c mice that were I.V. or I.T. injected with the LMM@BSA clay

503 nanosheets. A remarkable brightness intensity increase could be observed within the
504 tumor site after the I.V. (RBI: 1.6, Figure 6c-e) or I.T. (RBI: 2.7, Figure 6c,d,f) injection,
505 which provides the powerful proof for the promising in vivo MR imaging and
506 diagnosing of tumor.

507 **3.8. In vivo combined tumor therapy**

508 The tumor treatment effectiveness of LMM@BSA/Ce6 nanosheets was finally
509 verified on tumor-bearing mice (HT29 colorectal carcinoma, Figure 7). Due to the
510 photo-thermal efficiency, the tumor surface temperature of the mice with I.V. or I.T.
511 LMM@BSA injection raised by $\sim 16^{\circ}\text{C}$ or $\sim 33^{\circ}\text{C}$ upon the 5 min 808 nm laser
512 irradiation. However, no noticeable temperature changes were found in the control
513 group (Figure 7a). In vivo imaging of mice further proved the photo-thermal effect of
514 LMM@BSA and the neglectable thermal effect of saline (Figure 7c). Subsequently,
515 the therapy efficiency was monitored by measuring the tumor volume and recording
516 digital photographs (Figure 7b and d). The tumor volume of the control group was
517 about 5.7 ± 1.2 times larger than the original after 28 d feeding. After single laser
518 irradiation, the tumor expanded 3.0 ± 0.2 (660 nm) and 1.9 ± 0.1 times (808 nm) of its
519 volume after 28 d feeding, manifesting that the individual PTT or PDT therapy could
520 inhibit the tumor growth to some extent. Notably, the tumor volume shrank to
521 approximately 40% of the original (I.V. injection) and were eradicated (I.T. injection)
522 after the combined PDT and PTT, visually illustrating that the combination of
523 hyperthermia and ROS produced the excellent tumor restraining-effect.

524 **3.9. Drugs loading and releasing behaviors**

525 In addition to Ce6, the LMM@BSA clay nanosheets could also work as a carrier to

526 physically load antitumor drugs (e.g., DOX) and control its release. The optimized
527 DOX loading efficiency was calculated as 66.9%. The drug release pattern was
528 plotted by changing external conditions. The releasing rate was lower than 10% (6.2%)
529 in neutral condition (50°C). However, it was significantly improved in the acidic
530 condition (pH = 6.0), which reached 54.9% and 52.3% under 37°C and 54°C,
531 respectively (Figure S12). The DOX was also released more swiftly in higher
532 temperature, meaning that the NIR would promote the drug-releasing. This DOX
533 releasing kinetics with pH and temperature (NIR laser)-dependent properties could
534 equip the LMM@BSA clay nanosheets with competitiveness for tumor chemotherapy,
535 which would be discussed in the future study.

536

537 **4. Conclusion**

538 In summary, a novel kind of biocompatible Mg-Mn-Al LDH-based nano-platform,
539 namely LMM@BSA which could integrate the photo-thermal effect of MoS₂ was
540 synthesized using a hydrothermal approach. The surface of LMM was coated with
541 BSA to render it with excellent colloidal stability under physiological conditions. Owing
542 to the fast break-up in acidic conditions and the reduction of Mn³⁺ to Mn²⁺ by GSH in
543 tumor micro-environment, the MR imaging of Mg-Mn-Al LDH was strengthened.
544 Notably, the interlayer space and the surface of LMM@BSA clay nanosheets could be
545 used to efficiently load Ce6. The ROS production of Ce6 under the light irradiation
546 was distinctively enhanced since the LMM@BSA could catalyze the decomposing of
547 H₂O₂ in the tumor to produce oxygen. In addition, the high photo-thermal-conversion
548 efficiency of the MoS₂ component could elevate the local temperature of tumor, which

549 successfully achieved a remarkable PTT and PDT combined anticancer outcome.
550 This work presents an advances in the rational design of LDH-based
551 cancer-therapeutic modalities with simultaneous low side effects and high therapeutic
552 results.

553

554 **Supporting Information**

555 Supporting Information is available from the online or from the author.

556

557 **Author declaration**

558 All authors declare that they have no conflict of interest or financial conflicts to
559 disclose.

560

561 **Acknowledgements**

562 J. Z. and H. W. contributed equally to this work. This work was financially supported
563 by Medicine & Engineering Cross Research Foundation between Changhai Hosipital
564 and University of Shanghai for Science and Technology. Authors also thanks the
565 financial support of Shanghai Rising-Star Program (20QA1407200).

566

567 **References**

- 568 [1] K.D. Miller, L. Nogueira, A.B. Mariotto, J.H. Rowland, K.R. Yabroff, C.M. Alfano, A. Jemal,
569 J.L. Kramer, R.L. Siegel, Cancer treatment and survivorship statistics, 2019, Ca-Cancer J. Clin.,
570 10 (2019) 685-689.
- 571 [2] R.L. Siegel, K.D. Miller, S.A. Fedewa, D.J. Ahnen, R.G.S. Meester, A. Barzi, A. Jemal,
572 Colorectal cancer statistics, 2017, Ca-Cancer J. Clin., 67 (2017) 177-193.
- 573 [3] Y. Liu, Y. Xi, J. Zhao, J. Zhao, J. Li, G. Huang, J. Li, F. Fang, L. Gu, S. Wang, Preparation
574 of therapeutic-laden konjac hydrogel for tumor combination therapy, Chem. Eng. J., 375 (2019)

575 122048.

576 [4] A. Jemal, F. Bray, M.M. Center, J. Ferlay, E. Ward, D. Forman, Global cancer statistics,
577 *Ca-Cancer J. Clin.*, 61 (2011) 134.

578 [5] Q. Xiao, X. Zheng, W. Bu, W. Ge, S. Zhang, F. Chen, H. Xing, Q. Ren, W. Fan, K. Zhao, Y.
579 Hua, J. Shi, A core/satellite multifunctional nanotheranostic for in vivo imaging and tumor
580 eradication by radiation/photothermal synergistic therapy, *J. Am. Chem. Soc.*, 135 (2013)
581 13041-13048.

582 [6] T. Liu, C. Wang, W. Cui, H. Gong, C. Liang, X. Shi, Z. Li, B. Sun, Z. Liu, Combined photothermal
583 and photodynamic therapy delivered by PEGylated MoS₂ nanosheets, *Nanoscale*, 6 (2015)
584 11219-11225.

585 [7] T. Nakae, Y. Uto, M. Tanaka, H. Shibata, E. Nakata, M. Tominaga, H. Maezawa, T. Hashimoto,
586 K.L. Kirk, H. Nagasawa, H. Hori, Design, synthesis, and radiosensitizing activities of
587 sugar-hybrid hypoxic cell radiosensitizers, *Bioorgan Med. Chem.*, 16 (2008) 675-682.

588 [8] J.F. Hainfeld, F.A. Dilmanian, D.N. Slatkin, H.M. Smilowitz, Radiotherapy enhancement with
589 gold nanoparticles, *J. Pharm. Pharmacol.*, 60 (2008) 977-985.

590 [9] Y. Zheng, W. Wang, J. Zhao, C. Wu, C. Ye, M. Huang, S. Wang, Preparation of injectable
591 temperature-sensitive chitosan-based hydrogel for combined hyperthermia and chemotherapy of
592 colon cancer, *Carbohydr. Polym.*, 222 (2019) 115039.

593 [10] Y. Xu, J. Zhao, Z. Zhang, J. Zhang, M. Huang, S. Wang, P. Xie, Preparation of electrospray
594 ALG/PDA - PVP nanocomposites and their application in cancer therapy, *Soft Matter*, 16 (2019)
595 132-141.

596 [11] W. Li, X. Wang, J. Wang, Y. Guo, S.-Y. Lu, C.M. Li, Y. Kang, Z.-G. Wang, H.-T. Ran, Y.
597 Cao, H. Liu, Enhanced photoacoustic and photothermal effect of functionalized polypyrrole
598 nanoparticles for near-infrared theranostic treatment of tumor, *Biomacromolecules*, 20 (2019)
599 401-411.

600 [12] L. Lin, Z. Cong, J. Cao, K. Ke, Q. Peng, J. Gao, H. Yang, G. Liu, X. Chen, Multifunctional
601 Fe₃O₄@polydopamine core-shell nanocomposites for intracellular mRNA detection and
602 imaging-guided photothermal therapy, *ACS Nano*, 8 (2014) 3876-3883.

603 [13] B. Yang, Y. Chen, J. Shi, Material chemistry of two-dimensional inorganic nanosheets in
604 cancer theranostics, *Chem.*, 4 (2018) 1284-1313.

605 [14] D.K. Macharia, Q. Tian, L. Chen, Y. Sun, N. Yu, C. He, H. Wang, Z. Chen, PEGylated (NH₄)_xWO₃
606 nanorods as efficient and stable multifunctional nanoagents for simultaneous CT imaging and
607 photothermal therapy of tumor, *J. Photoch. Photobio. B.*, 174 (2017) 10-17.

608 [15] B. Liu, C. Li, G. Chen, B. Liu, X. Deng, Y. Wei, J. Xia, B. Xing, P.a. Ma, J. Lin, Synthesis
609 and optimization of MoS₂@Fe₃O₄-ICG/Pt(IV) nanoflowers for MR/IR/PA boimaging and combined
610 PTT/PDT/chemotherapy triggered by 808 nm laser, *Adv. Sci.*, 4 (2017) 1600540.

611 [16] S. Gao, H.L. Zhou, S.M. Cui, H. Shen, Bottom-up synthesis of MoS₂ nanospheres for
612 photothermal treatment of tumors, *Photoch. Photobio. Sci.*, 17 (2018) 1337-1345.

613 [17] J. Wei, J. Li, D. Sun, Q. Li, J. Ma, X. Chen, X. Zhu, N. Zheng, A novel theranostic
614 nanoplatfom based on Pd@Pt-PEG-Ce6 for enhanced photodynamic therapy by modulating tumor
615 Hypoxia microenvironment, *Adv. Funct. Mater.*, 28 (2018) 1-12.

616 [18] W.-S. Kuo, C.-N. Chang, Y.-T. Chang, M.-H. Yang, Y.-H. Chien, S.-J. Chen, C.-S. Yeh, Gold
617 nanorods in photodynamic therapy, as hyperthermia agents, and in near-infrared optical imaging,
618 *Angew. Chem. Int. Ed.*, 49 (2010) 2711-2715.

619 [19] J. Wang, G. Zhu, M. You, E. Song, M.I. Shukoor, K. Zhang, M.B. Altman, Y. Chen, Z. Zhu,

620 C. Z. Huang, W. Tan, Assembly of aptamer switch probes and photosensitizer on gold nanorods for
621 targeted photothermal and photodynamic cancer therapy, *ACS Nano*, 6 (2012) 5070–5077.

622 [20] L. Gao, J. Fei, J. Zhao, H. Li, Y. Cui, J. Li, Hypocrellin-loaded gold nanocages with high
623 two-photon efficiency for photothermal/hotodynamic cancer therapy in vitro, *ACS Nano*, 6 (2012)
624 8030–8040.

625 [21] B. Jang, J.-Y. Park, C.-H. Tung, I.-H. Kim, Y. Choi, Gold nanorod–photosensitizer complex
626 for near-infrared fluorescence imaging and photodynamic/photothermal therapy in vivo, *ACS Nano*,
627 5 (2011) 1086–1094.

628 [22] B. Tian, C. Wang, S. Zhang, L. Feng, Z. Liu, Photothermally enhanced photodynamic therapy
629 delivered by nano-graphene oxide, *ACS Nano*, 5 (2011) 7000–7009.

630 [23] Z. Chen, Z. Li, J. Wang, E. Ju, L. Zhou, J. Ren, X. Qu, A multi-synergistic platform for
631 sequential irradiation-activated high-performance apoptotic cancer therapy, *Adv. Funct. Mater.*,
632 24 (2014) 522–529.

633 [24] F. Li, S.-J. Park, D. Ling, W. Park, J.Y. Han, K. Na, K. Char, Hyaluronic acid-conjugated
634 graphene oxide/photosensitizer nanohybrids for cancer targeted photodynamic therapy, *J. Mater.*
635 *Chem. B*, 1 (2013) 1678–1686.

636 [25] H. Gong, L. Cheng, J. Xiang, H. Xu, L. Feng, X. Shi, Z. Liu, Near-infrared absorbing polymeric
637 nanoparticles as a versatile drug carrier for cancer combination therapy, *Adv Funct Mater*, 23
638 (2013) 6059–6067.

639 [26] S.P. Sherlock, S.M. Tabakman, L. Xie, H. Dai, Photothermally enhanced drug delivery by
640 ultrasmall multifunctional feco/graphitic shell nanocrystals, *ACS Nano*, 5 (2011) 1505–1512.

641 [27] K. Dong, Z. Liu, Z. Li, J. Ren, X. Qu, Hydrophobic anticancer drug delivery by a 980 nm
642 laser-driven photothermal vehicle for efficient synergistic therapy of cancer cells in vivo,
643 *Adv. Mater.*, 25 (2013) 4452–4458.

644 [28] P. Mi, D. Kokuryo, H. Cabral, H.L. Wu, Y. Terada, T. Saga, I. Aoki, N. Nishiyama, K. Kataoka,
645 A pH-activatable nanoparticle with signal-amplification capabilities for non-Invasive imaging
646 of tumour malignancy, *Nat Nanotechnol*, 11 (2016) 724.

647 [29] B. Guo, J. Zhao, Z. Zhang, X. An, M. Huang, S. Wang, Intelligent nanoenzyme-based theranostic
648 agent for T₁-weighted MR imaging and combined tumor photo-therapy *Chem. Eng. J.*, 382 (2020)
649 123609.

650 [30] J. Wang, X. Wang, S.-Y. Lu, J. Hu, W. Zhang, L. Xu, D. Gu, W. Yang, W. Tang, F. Liu, Y.
651 Cao, H. Liu, Integration of cascade delivery and tumor hypoxia modulating capacities in
652 core-releasable satellite nanovehicles to enhance tumor chemotherapy, *Biomaterials*, 223 (2019)
653 119465.

654 [31] N. Khatoon, M.Q. Chu, C.H. Zhou, Nanoclay-based drug delivery systems and their therapeutic
655 potentials, *J. Mater. Chem. B*, 8 (2020) 7335–7351.

656 [32] S. Wang, L. Zhou, Y. Zheng, L. Li, C. Wu, H. Yang, M. Huang, X. An, Synthesis and
657 biocompatibility of two-dimensional biomaterials, *Colloid Surface A*, 583 (2019) 124004.

658 [33] Q. Wang, D. O’ Hare, Recent Advances in the Synthesis and Application of Layered Double
659 Hydroxide (LDH) Nanosheets, *Chemical Reviews*, 112 (2012) 4124–4155.

660 [34] M.-Q. Zhao, Q. Zhang, J.-Q. Huang, F. Wei, Hierarchical nanocomposites derived from
661 nanocarbons and layered double hydroxides—properties, synthesis, and applications, *Adv. Funct.*
662 *Mater.*, 22 (2012) 675–694.

663 [35] J. Ma, P. Duan, D. Ren, W. Zhou, Effects of layered double hydroxides incorporation on

664 carbonation resistance of cementitious materials, *J. Mater. Res. Technol.*, 8 (2019) 292–298.
665 [36] D.G. Evans, X. Duan, Preparation of layered double hydroxides and their applications as
666 additives in polymers, as precursors to magnetic materials and in biology and medicine, *Chem.*
667 *Commun.*, (2006) 485–496.
668 [37] G.R. Williams, D. O’Hare, Towards understanding, control and application of layered double
669 hydroxide chemistry, *J. Mater. Chem. B.*, 16 (2006) 3065–3074.
670 [38] A.I. Khan, D. O’Hare, Intercalation chemistry of layered double hydroxides: Recent
671 developments and applications, *J. Mater. Chem. B.*, 12 (2002) 3191–3198.
672 [39] M.J. Barnabas, S. Parambadath, S. Nagappan, C.-S. Ha, Sulfamerazine schiff-base complex
673 intercalated layered double hydroxide: synthesis, characterization, and antimicrobial activity,
674 *Heliyon*, 5 (2019) e01521.
675 [40] W. Yang, W. Guo, J. Chang, B. Zhang, Protein/peptide-templated biomimetic synthesis of
676 inorganic nanoparticles for biomedical applications, *J. Mater. Chem. B*, 5 (2017) 401–417.
677 [41] W. Feng, X. Han, R. Wang, X. Gao, P. Hu, W. Yue, Y. Chen, J. Shi, Nanocatalysts-augmented
678 and photothermal-enhanced tumor-specific sequential nanocatalytic therapy in both NIR-I and
679 NIR-II biowindows, *Adv. Mater.*, 31 (2019) 1805919.
680 [42] Q. Tian, J. Hu, Y. Zhu, R. Zou, Z. Chen, S. Yang, R. Li, Q. Su, Y. Han, X. Liu, Sub-10
681 nm Fe₃O₄@Cu_{2-x}S core-shell nanoparticles for dual-modal imaging and photothermal therapy, *J. Am.*
682 *Chem. Soc.*, 135 (2013) 8571–8577.
683 [43] Y. Zhao, F. Li, R. Zhang, D.G. Evans, X. Duan, Preparation of layered double-hydroxide
684 nanomaterials with a uniform crystallite size using a new method involving separate nucleation
685 and aging steps, *Chem. Mater.*, 14 (2002) 4286–4291.
686 [44] S. Li, Y. Guo, M. Xiao, T. Zhang, S. Yao, S. Zang, H. Fan, Y. Shen, Z. Zhang, W. Li, Enhanced
687 arsenate removal from aqueous solution by Mn-doped MgAl-layered double hydroxides, *Environ.*
688 *Sci. Pollut. R.*, 26 (2019) 12014–12024.
689 [45] T. Liu, C. Wang, X. Gu, H. Gong, L. Cheng, X. Shi, L. Feng, B. Sun, Z. Liu, Drug delivery
690 with PEGylated MoS₂ nano-sheets for combined photothermal and chemotherapy of cancer, *Adv. Mater.*,
691 26 (2014) 3433–3440.
692 [46] W. Yin, L. Yan, J. Yu, G. Tian, L. Zhou, X. Zheng, X. Zhang, Y. Yong, J. Li, Z. Gu, Y.
693 Zhao, High-throughput synthesis of single-layer MoS₂ nanosheets as a near-infrared
694 photothermal-triggered drug delivery for effective cancer therapy, *ACS Nano*, 8 (2014) 6922–6933.

695

696

697

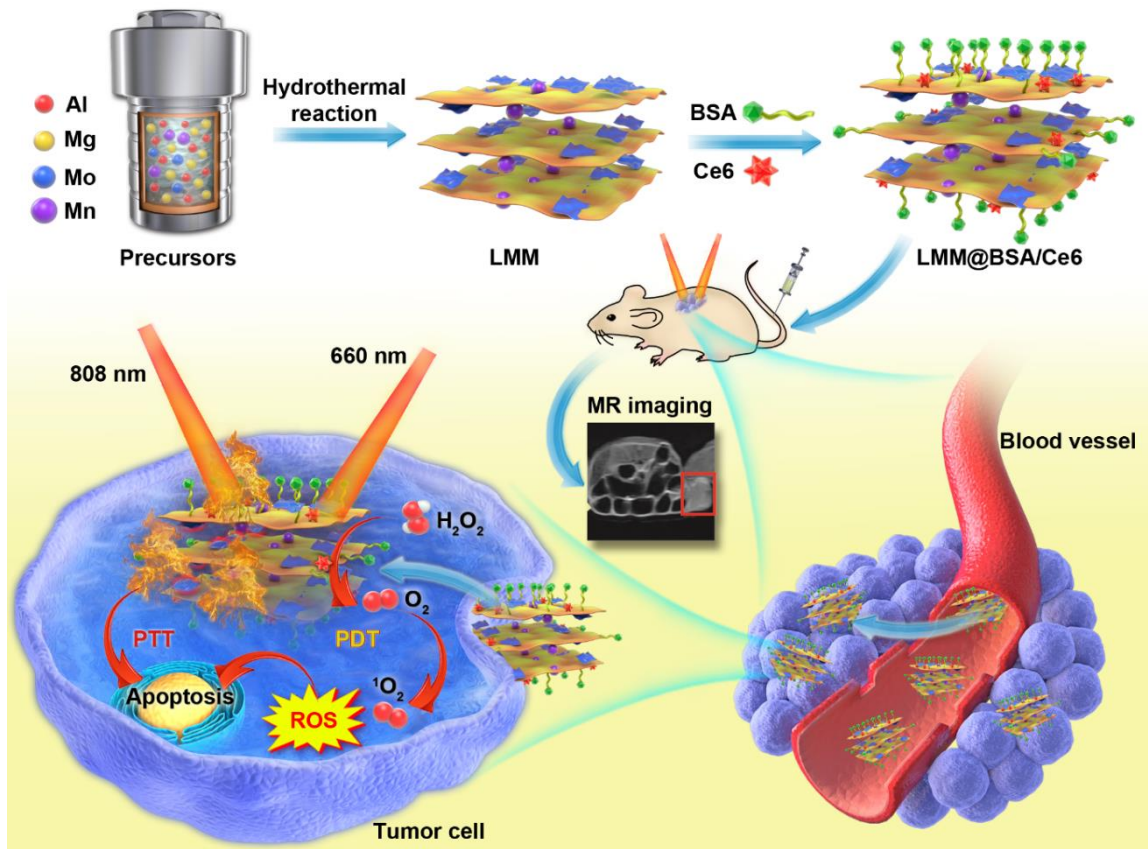
698

699

700

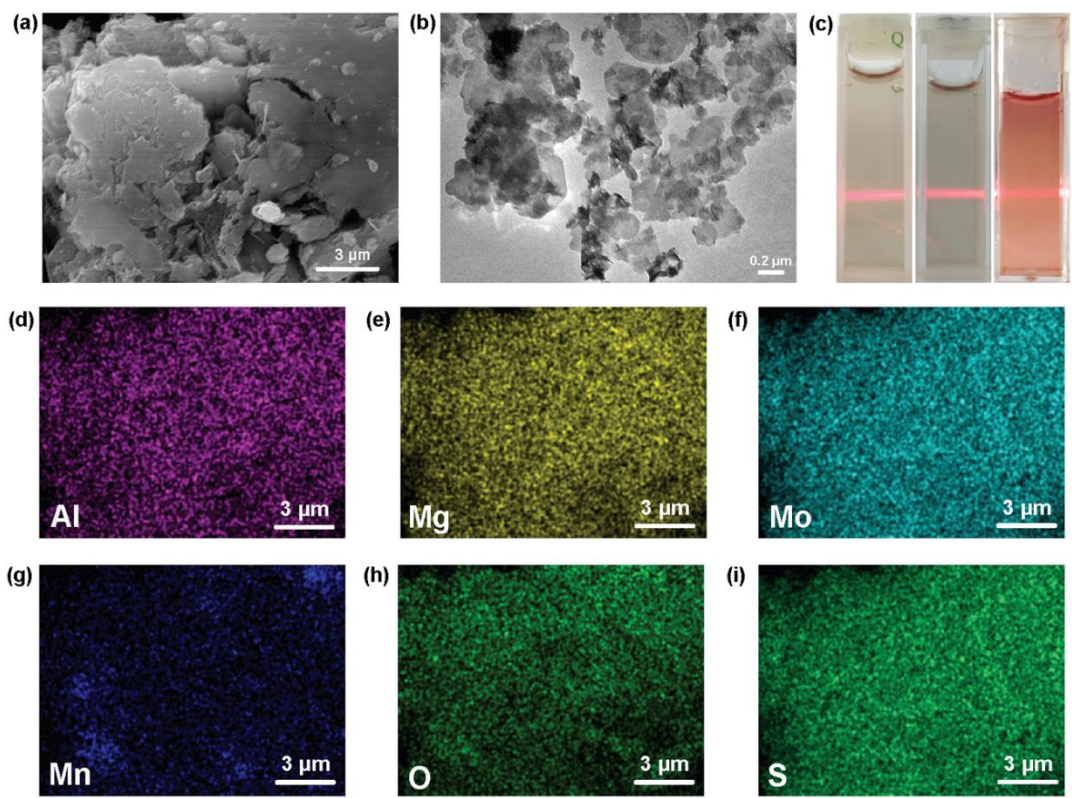
701

702 **Figures**



703

704 **Scheme 1.** Schematic illustration of the hydrothermal synthesis with BSA coating and
705 Ce6 loading and the synergistic tumor photo-therapy procedure of LMM@BSA/Ce6
706 nanosheets simultaneously including catalase-mimic and imaging-guided capacity.



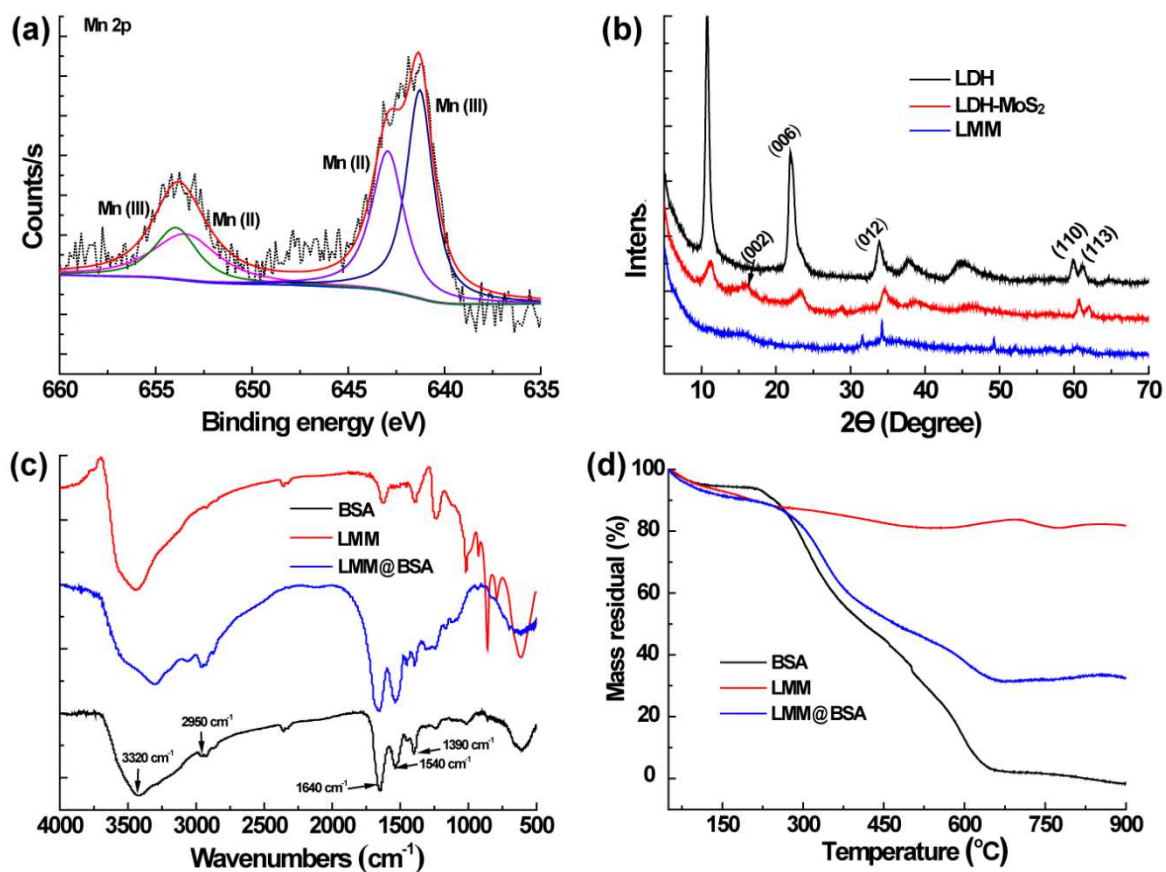
707

708 **Figure 1** (a) SEM of LMM nanosheets; (b) TEM of LMM@BSA clay nanosheets; (c)

709 photographic image of typical Tyndall phenomenon of LMM@BSA clay nanosheets in

710 water (left), saline (middle), and DMEM (right); (d-i) Al, Mg, Mo, Mn, O and S

711 elemental distribution mappings of LMM nanosheets.

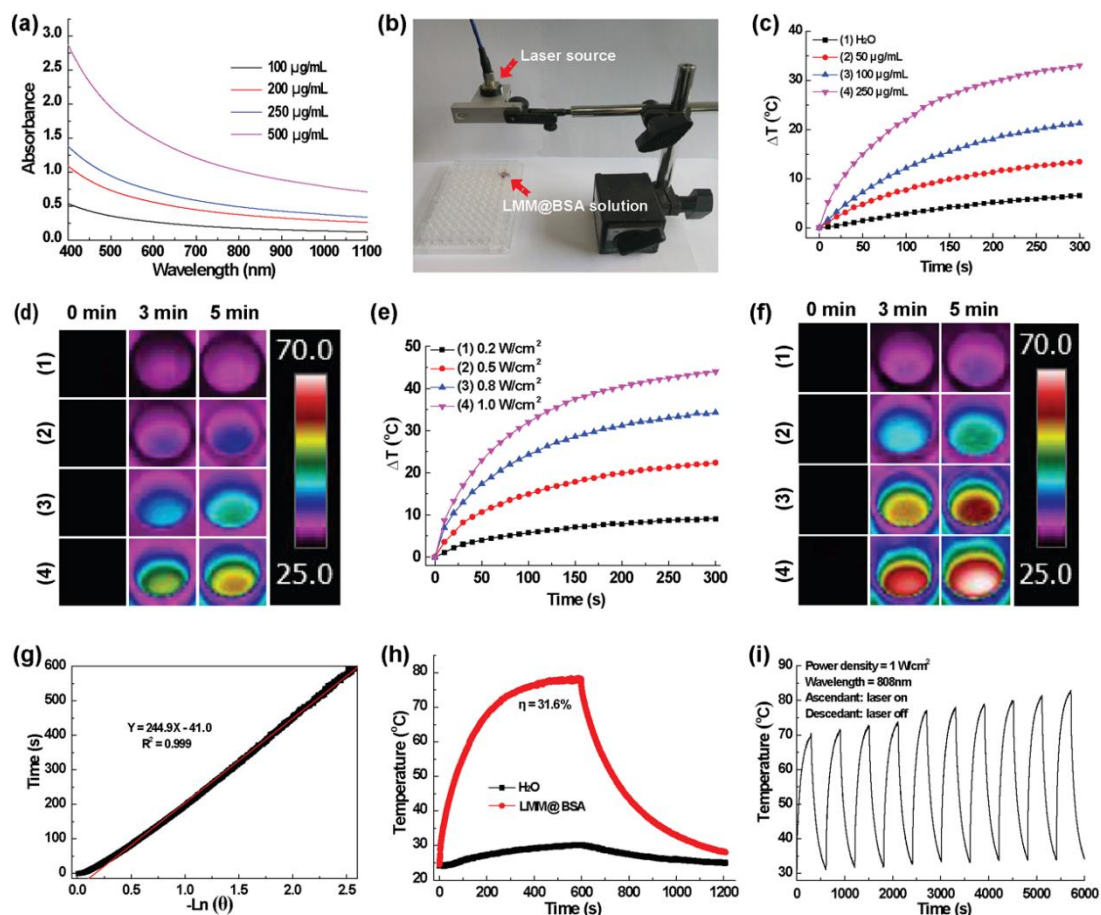


712

713 **Figure 2** (a) XPS spectrum of Mn 2p; (b) XRD patterns of LDH, LDH-MoS₂, and LMM

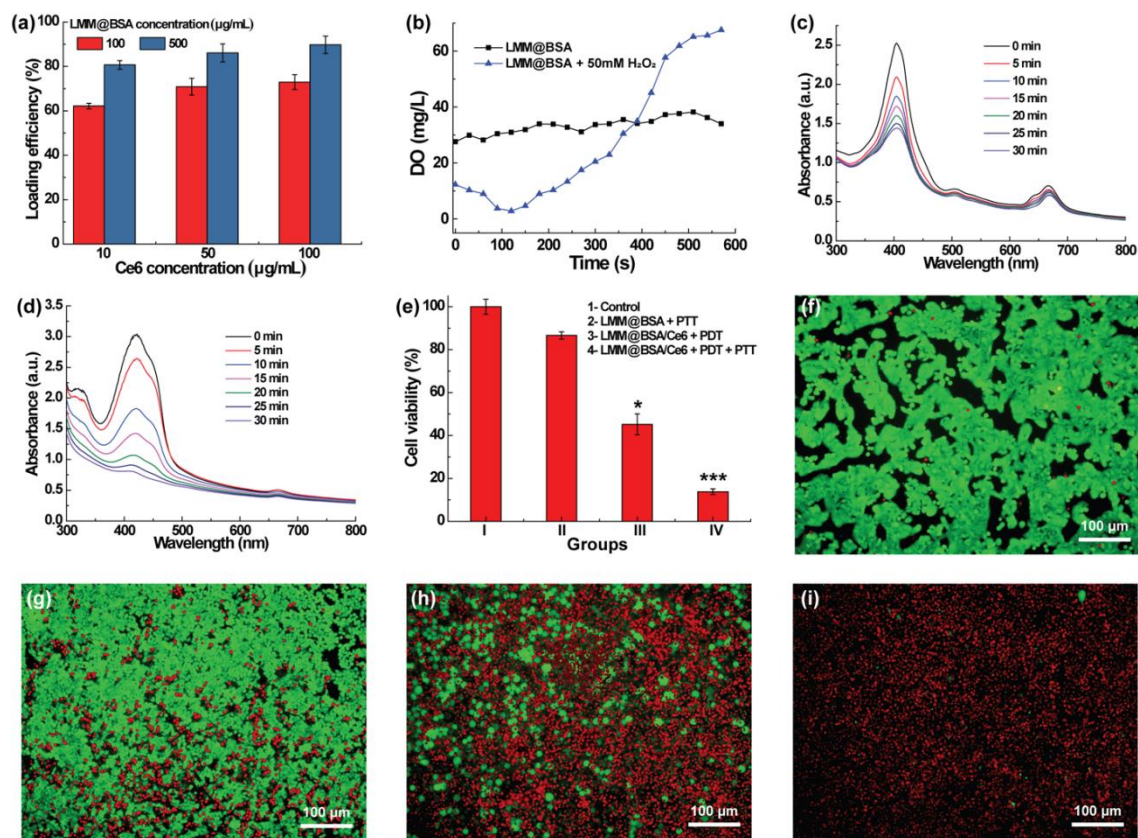
714 nanosheets; (c) FTIR spectra of LDH, LMM, and LMM@BSA nanosheets; (e) TG

715 curves of LDH, LMM, and LMM@BSA nanosheets.



716

717 **Figure 3** (a) Light absorption of LMM@BSA clay nanosheets solution; (b) the
 718 photograph of the experimental appliance; (c) distilled water and
 719 concentration-dependent temperature profiles of LMM@BSA clay nanosheets (NIR
 720 laser: 1W/cm²); (d) corresponding thermal imaging of (c); (e) power
 721 density-dependent temperature profiles of LMM@BSA clay nanosheets solution; (f)
 722 corresponding thermal imaging of (e); (g) time constant for heat transfer of
 723 LMM@BSA clay nanosheets; (h) steady-state heating curve of LMM@BSA clay
 724 nanosheets and distilled water and (i) recycling heating profiles of LMM@BSA clay
 725 nanosheets. The unit of bar in (d) and (f) is °C.



726

727 **Figure 4** (a) The Ce6 loading efficiency of LMM@BSA clay nanosheets with different

728 concentrations; (b) the DO content of dissolved oxygen in LMM@BSA and

729 LMM@BSA + H₂O₂ solution; (c, d) absorption spectrum changes of DPBF under 660

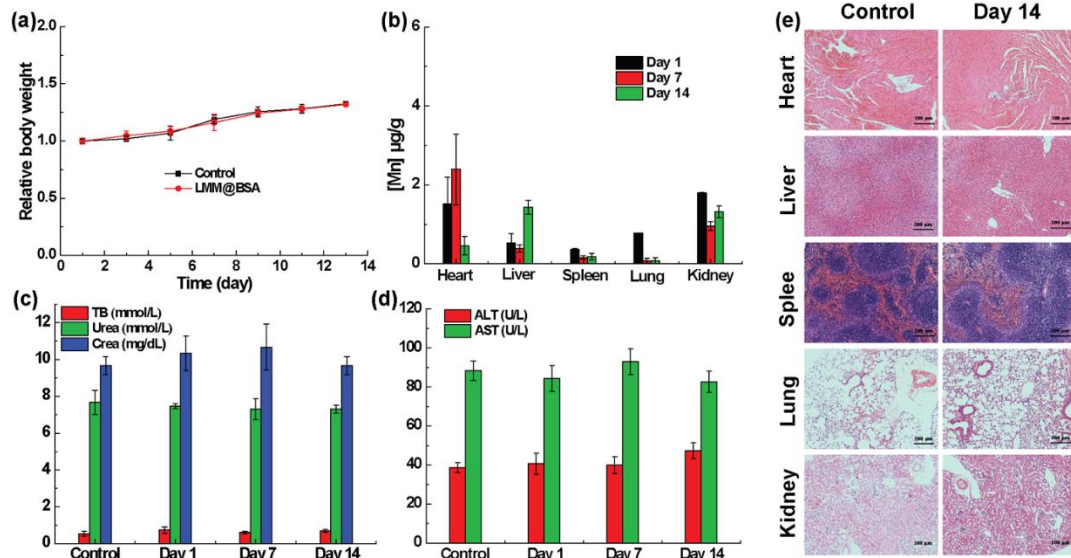
730 nm laser irradiation with LMM@BSA/Ce6 nanosheets (c) in the absence and (d)

731 presence of H₂O₂ (10 mM); (e) viability profile of HT29 cells after synergistic treatment;

732 (f-i) the calcein-AM/PI dyeing morphology of HT29 cells corresponding to (e): (f)

733 control; (g) LMM@BSA + PTT; (h) LMM@BSA/Ce6 + PDT ; (i) LMM@BSA/Ce6 +

734 PDT + PTT.



735

736 **Figure 5** (a) The relative body weight changes of KM mice treated with saline and

737 LMM@BSA clay nanosheets (n = 3); (b) long-term Mn bio-distribution of mice injected

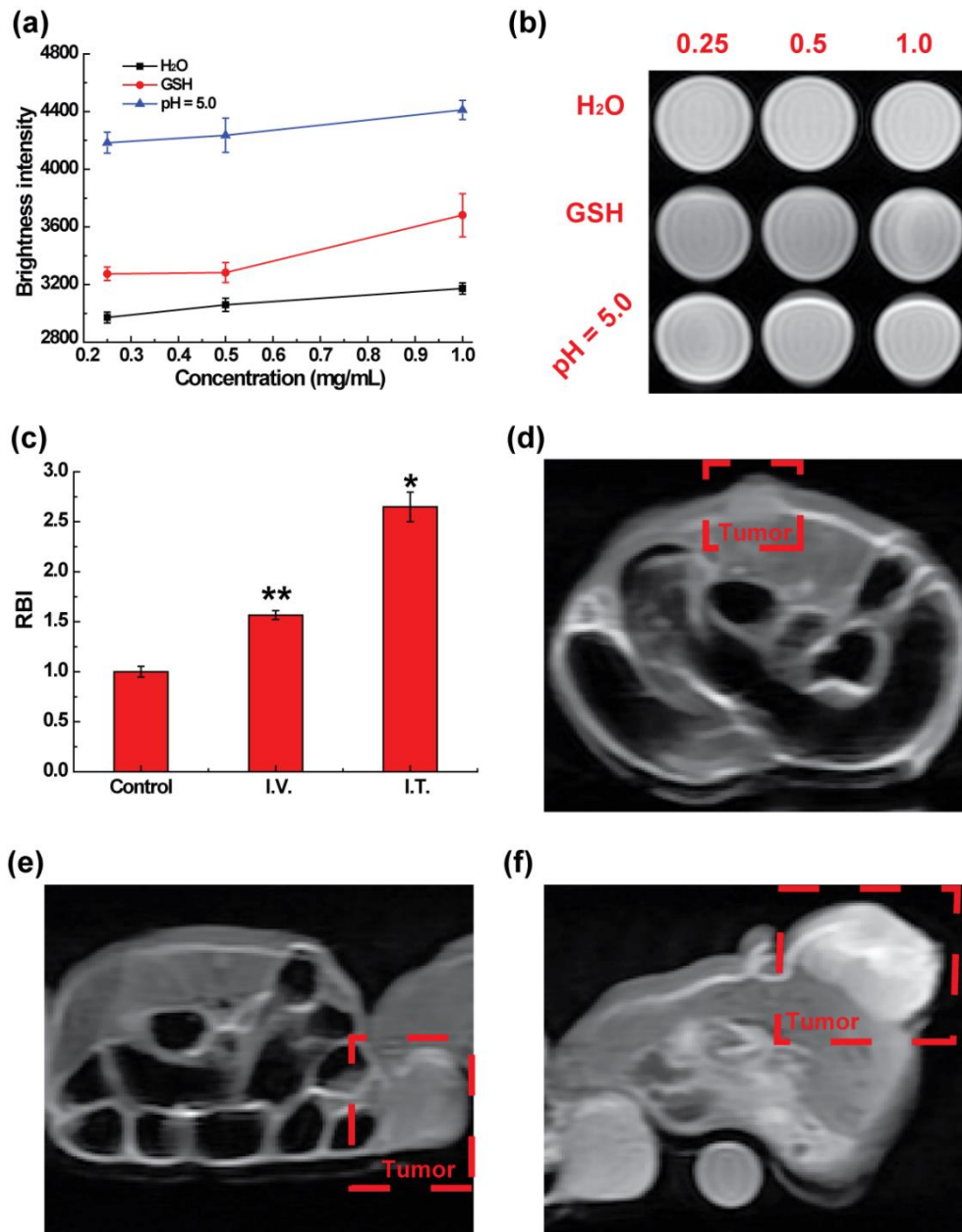
738 with LMM@BSA/Ce6 nanosheets; (c, d) serum biochemistry assay of mice injected

739 with saline (control) and LMM@BSA dispersion and fed for different days. TB: total

740 bilirubin; CREA: Creatinine; ALT: alanine transaminase; AST: amino-transferase; (e)

741 H&E-dyed tissue sections of major organs of KM mice that injected with saline or

742 LMM@BSA clay nanosheets and fed for 14 days (Scale = 100 μm).



743

744 **Figure 6** (a) In vitro brightness intensity of LMM@BSA in a mildly acidic environment

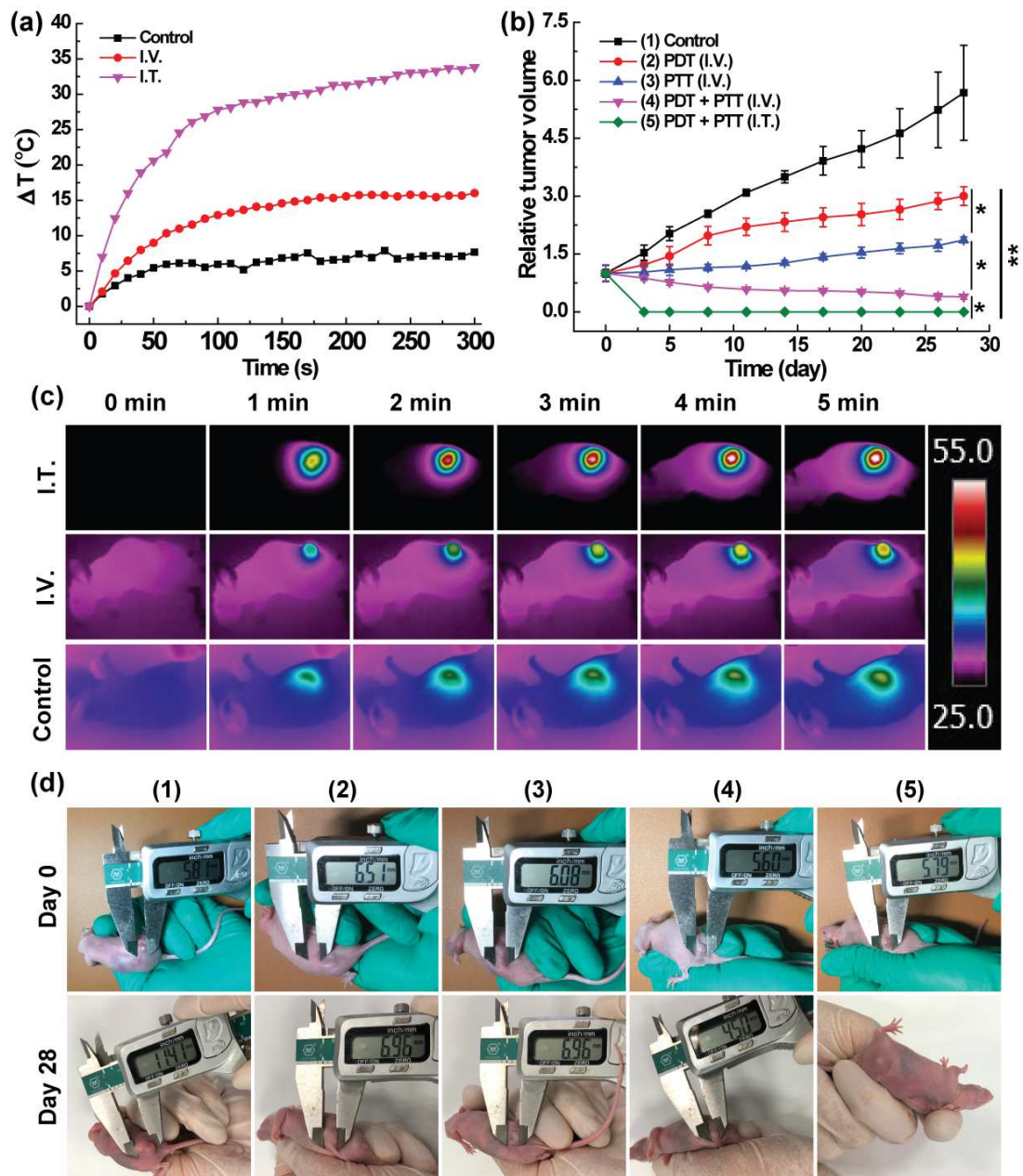
745 (pH = 5.0), distilled water or GSH aqueous solutions after soaking at 37 °C for 2h; (b)

746 T₁-weighted MR imaging of solution corresponding to (a); (c) in vivo relative

747 brightness intensity of mice tumor after I.T. or I.V. injected with saline and LMM@BSA;

748 (d-f) in vivo T₁-weighted MR imaging corresponded to (c): (d): control, (e): I.V., and (f)

749 I.T..



750

751 **Figure 7** (a) The tumor heating curves of mice under NIR laser irradiation; (b) tumor

752 growth profile of mice after various treatments as noted; (c) in vivo thermal imaging of

753 mice after laser irradiation for different time points corresponding to (a); (d) pictures of

754 HT29 tumor-bearing mice at day 0 and day 28 corresponding to (b). The unit of the

755 bar in panel (c): °C.

Figures

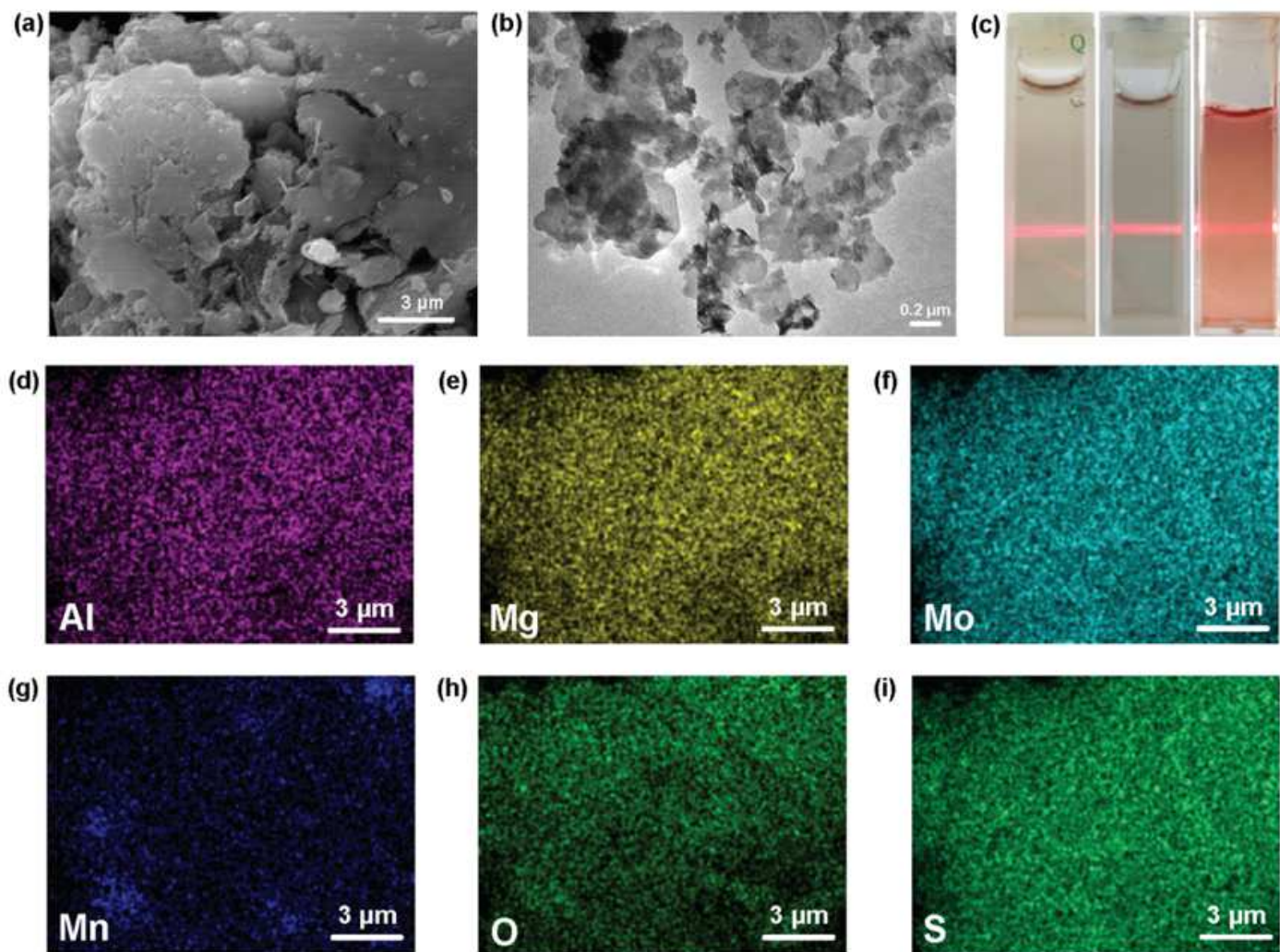


Figure 1

(a) SEM of LMM nanosheets; (b) TEM of LMM@BSA clay nanosheets; (c) photographic image of typical Tyndall phenomenon of LMM@BSA clay nanosheets in water (left), saline (middle), and DMEM (right); (d-i) Al, Mg, Mo, Mn, O and S elemental distribution mappings of LMM nanosheets.

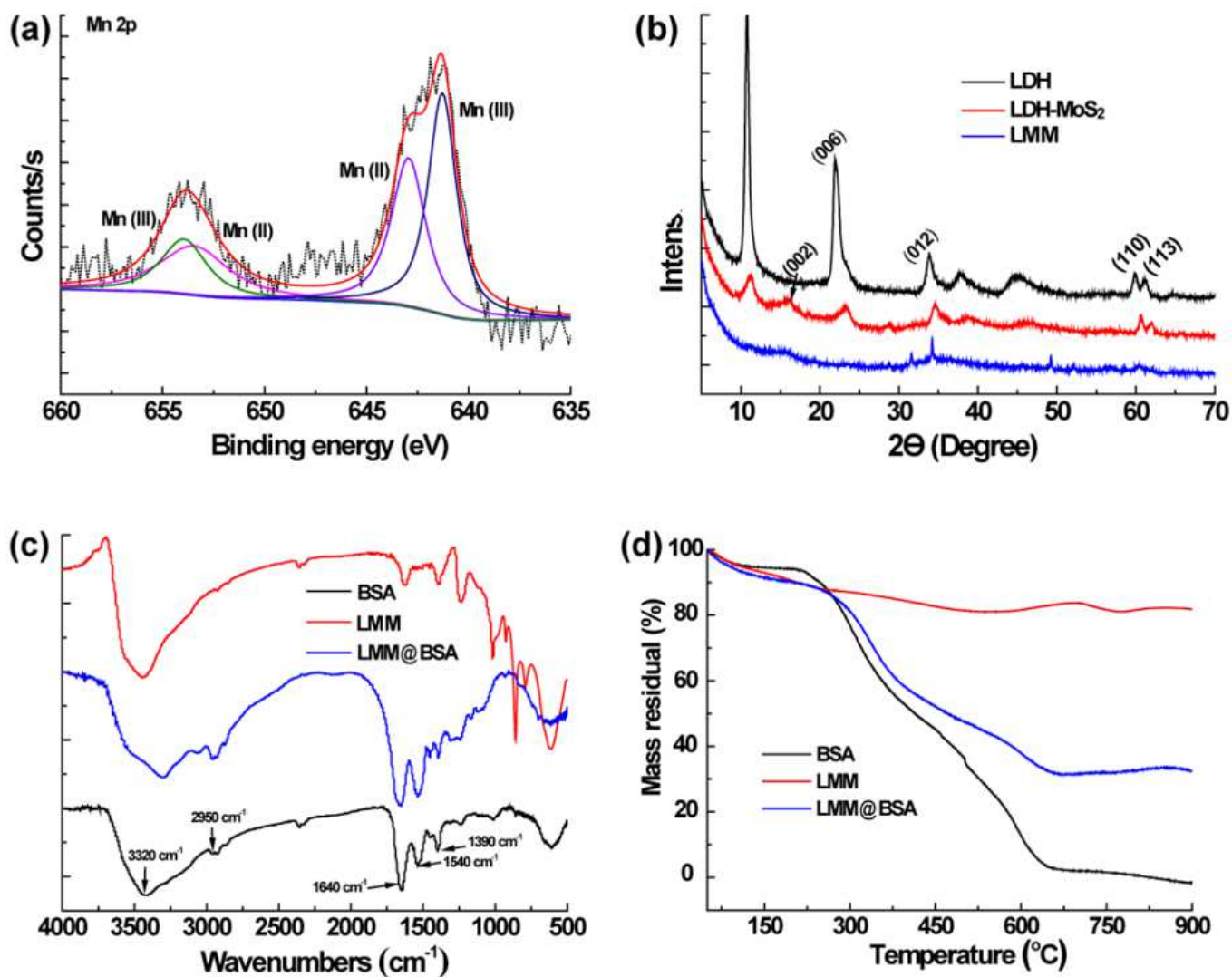


Figure 2

(a) XPS spectrum of Mn 2p; (b) XRD patterns of LDH, LDH-MoS₂, and LMM nanosheets; (c) FTIR spectra of LDH, LMM, and LMM@BSA nanosheets; (e) TG curves of LDH, LMM, and LMM@BSA nanosheets.

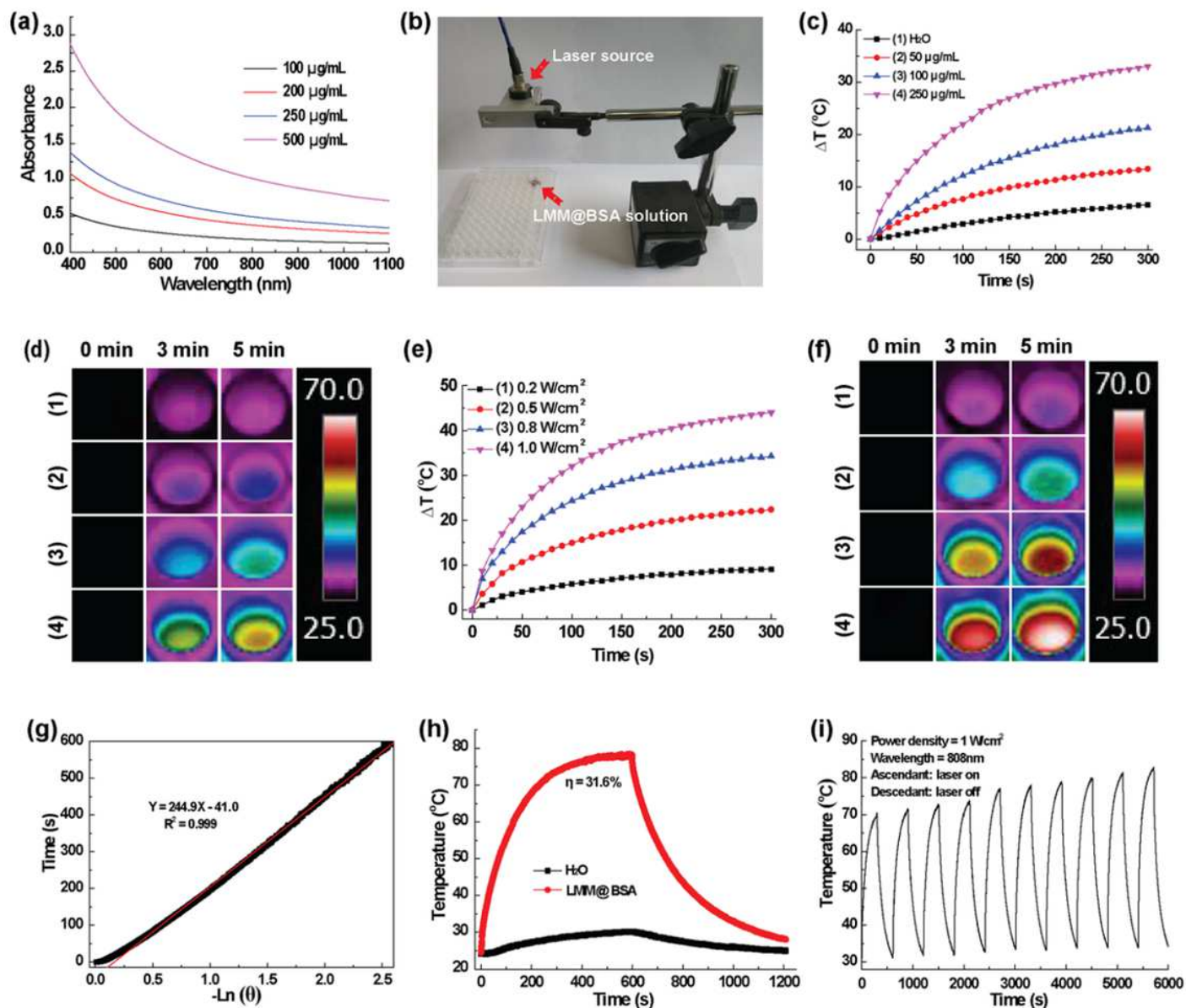


Figure 3

(a) Light absorption of LMM@BSA clay nanosheets solution; (b) the photograph of the experimental appliance; (c) distilled water and concentration-dependent temperature profiles of LMM@BSA clay nanosheets (NIR laser: 1W/cm²); (d) corresponding thermal imaging of (c); (e) power density-dependent temperature profiles of LMM@BSA clay nanosheets solution; (f) corresponding thermal imaging of (e); (g) time constant for heat transfer of LMM@BSA clay nanosheets; (h) steady-state heating curve of LMM@BSA clay nanosheets and distilled water and (i) recycling heating profiles of LMM@BSA clay nanosheets. The unit of bar in (d) and (f) is oC.

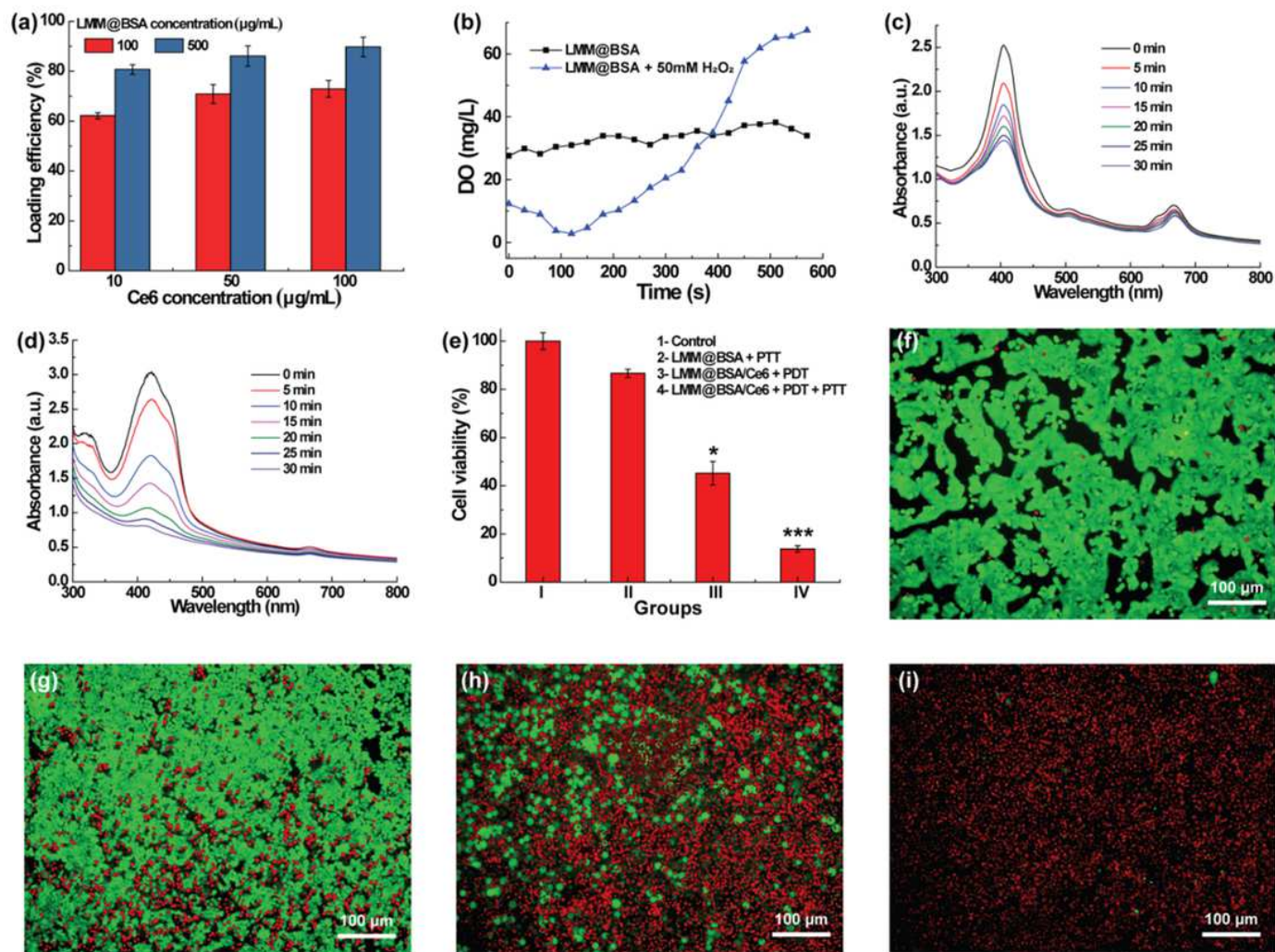


Figure 4

(a) The Ce6 loading efficiency of LMM@BSA clay nanosheets with different concentrations; (b) the DO content of dissolved oxygen in LMM@BSA and LMM@BSA + H₂O₂ solution; (c, d) absorption spectrum changes of DPBF under 660 nm laser irradiation with LMM@BSA/Ce6 nanosheets (c) in the absence and (d) presence of H₂O₂ (10 mM); (e) viability profile of HT29 cells after synergistic treatment; (f-i) the calcein-AM/PI dyeing morphology of HT29 cells corresponding to (e): (f) control; (g) LMM@BSA + PTT; (h) LMM@BSA/Ce6 + PDT ; (i) LMM@BSA/Ce6 + PDT + PTT.

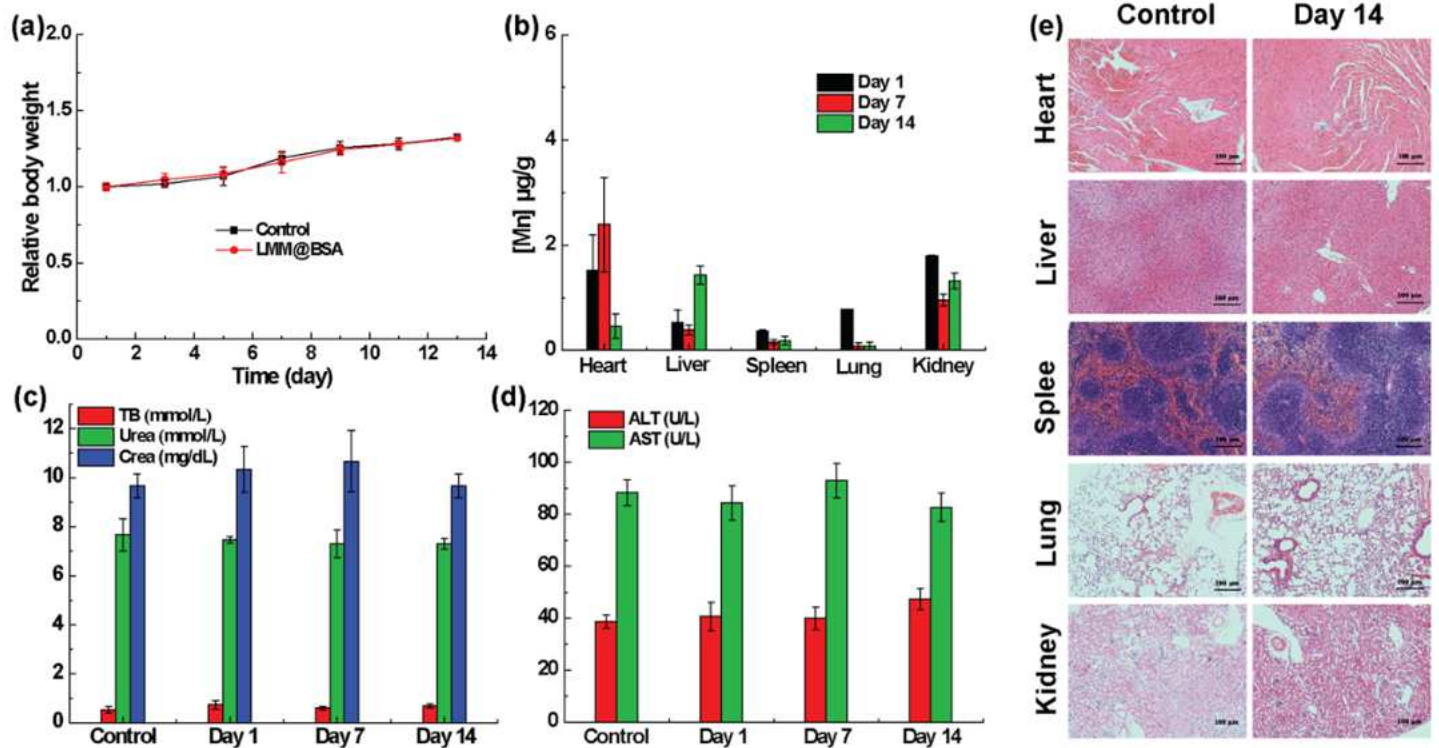


Figure 5

(a) The relative body weight changes of KM mice treated with saline and LMM@BSA clay nanosheets ($n = 3$); (b) long-term Mn bio-distribution of mice injected with LMM@BSA/Ce6 nanosheets; (c, d) serum biochemistry assay of mice injected with saline (control) and LMM@BSA dispersion and fed for different days. TB: total bilirubin; CREA: Creatinine; ALT: alanine transaminase; AST: amino-transferase; (e) H&E-dyed tissue sections of major organs of KM mice that injected with saline or LMM@BSA clay nanosheets and fed for 14 days (Scale = 100 µm).

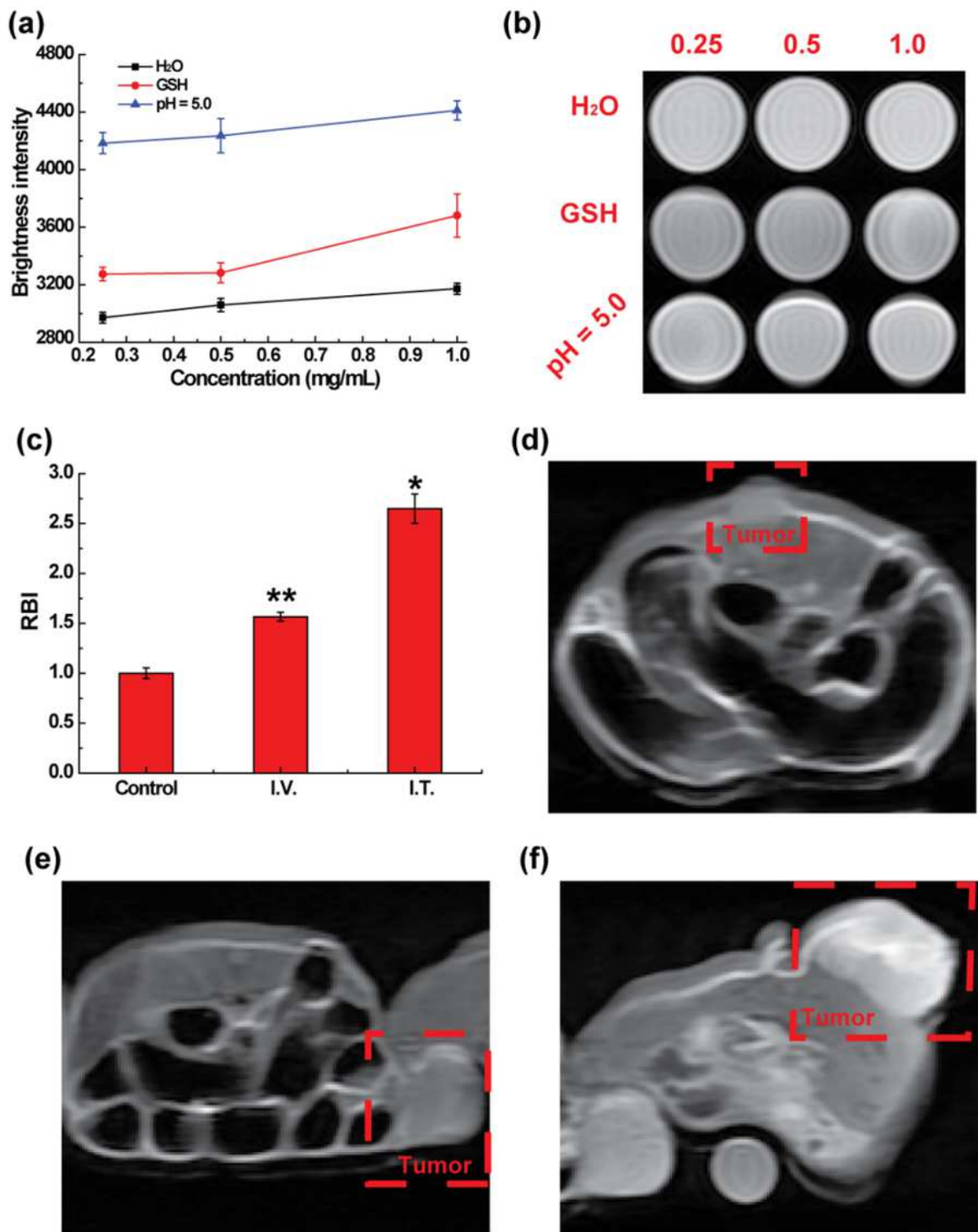


Figure 6

(a) In vitro brightness intensity of LMM@BSA in a mildly acidic environment (pH = 5.0), distilled water or GSH aqueous solutions after soaking at 37°C for 2h; (b) T1-weighted MR imaging of solution corresponding to (a); (c) in vivo relative brightness intensity of mice tumor after I.T. or I.V. injected with saline and LMM@BSA; (d-f) in vivo T1-weighted MR imaging corresponded to (c): (d): control, (e): I.V., and (f) I.T..

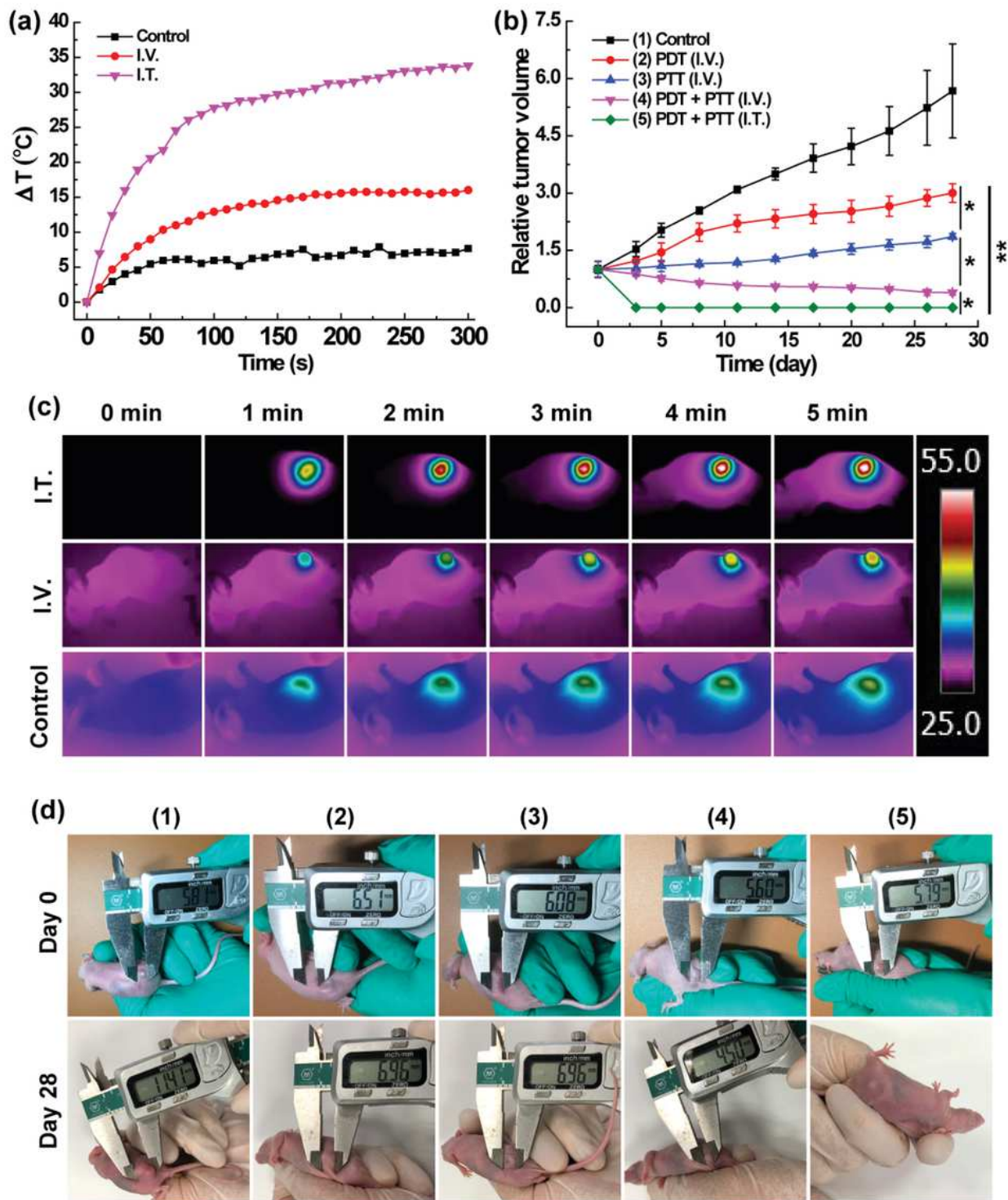


Figure 7

(a) The tumor heating curves of mice under NIR laser irradiation; (b) tumor growth profile of mice after various treatments as noted; (c) in vivo thermal imaging of mice after laser irradiation for different time points corresponding to (a); (d) pictures of HT29 tumor-bearing mice at day 0 and day 28 corresponding to (b). The unit of the bar in panel (c): °C.

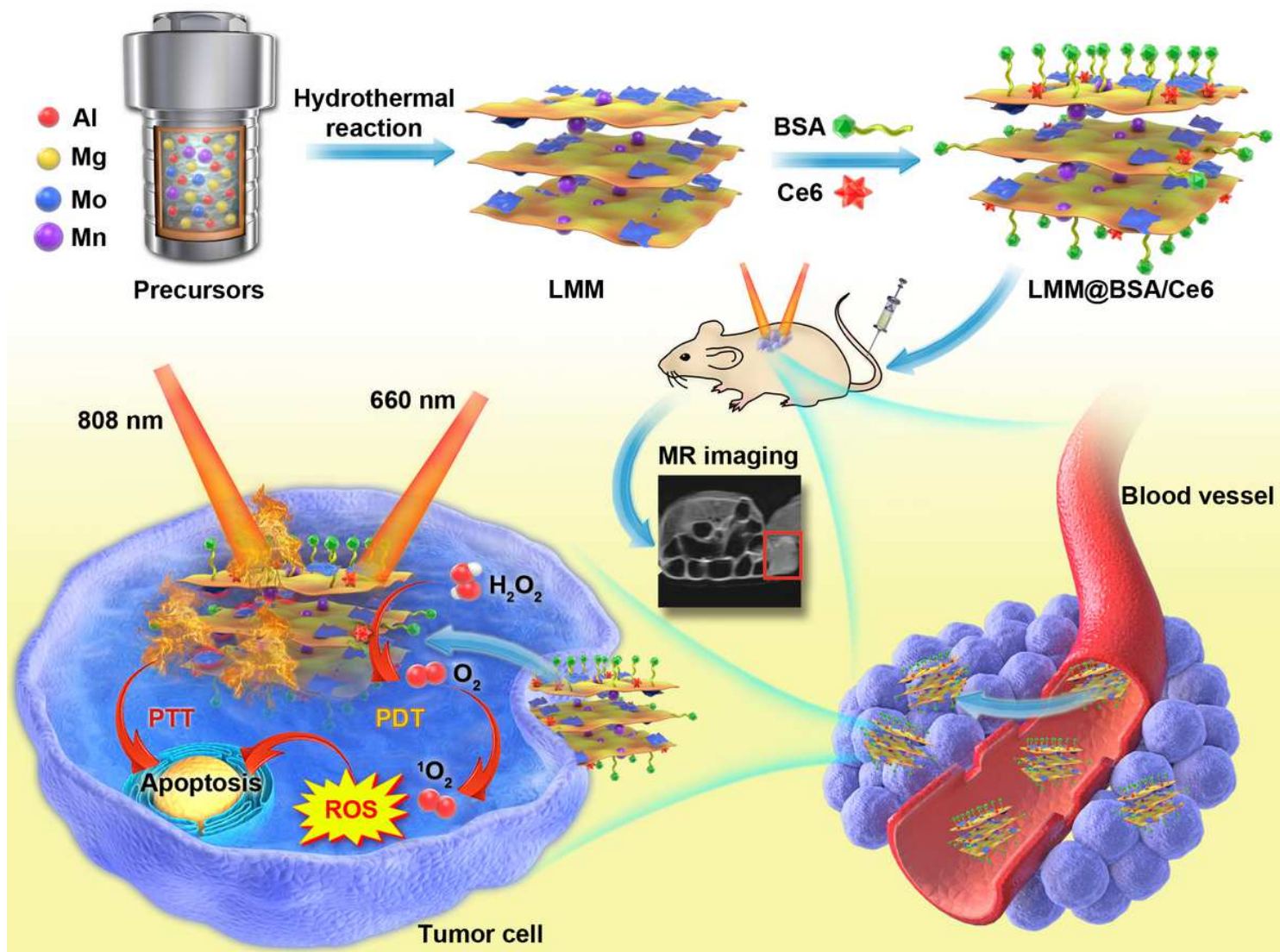


Figure 8

Scheme 1. Schematic illustration of the hydrothermal synthesis with BSA coating and Ce6 loading and the synergistic tumor photo-therapy procedure of LMM@BSA/Ce6 nanosheets simultaneously including catalase-mimic and imaging-guided capacity.

Supplementary Files

This is a list of supplementary files associated with this preprint. Click to download.

- [LMMBSASI.docx](#)